CHAPTER 9

Deformable Particles: Modeling and Applications

ARTHUR K. MACKEITH, a,b DONG WANG, MARK D. SHATTUCK AND COREY S. O'HERN*a,b,d

^a Department of Mechanical Engineering, Yale University, New Haven, Connecticut 06520, USA; ^b Integrated Graduate Program in Physical and Engineering Biology, Yale University, New Haven, Connecticut 06520, USA; ^c Benjamin Levich Institute and Physics Department, The City College of New York, New York, New York 10031, USA; ^d Department of Physics, Yale University, New Haven, Connecticut 06520, USA *Email: corey.ohern@yale.edu

9.1 Introduction

Particle shape changes occur in many particulate materials, especially in soft matter systems, such as colloids, foams, bubbles, and tissues, since the characteristic stresses that these particles experience are comparable to their elastic moduli. Particle shape changes play an important role in the spatiotemporal dynamics of soft particulate systems, including white blood cells crawling through the extracellular matrix, capillary droplets flowing through obstacle arrays, and soft granular particles undergoing cyclic shear. Particle deformation allows particles to remain mobile and undergo rearrangements with neighboring particles even when the system is confluent. Explicitly modeling particle shape changes is necessary to understand flow and clogging in microfluidic devices, collective cell motion and stress transmission in confluent tissues, and frictional particle interactions in MEMS devices.

Theoretical and Computational Chemistry Series No. 27 Packing Problems in Soft Matter Physics: Fundamentals and Applications Edited by Ho-Kei Chan, Stefan Hutzler, Adil Mughal, Corey S. O'Hern, Yujie Wang and Denis Weaire

[©] The Royal Society of Chemistry 2025 Published by the Royal Society of Chemistry, www.rsc.org

The mechanics that govern particle shape changes can be elastic, surfaceenergy dominated, and plastic, as well as intermediate mechanical behavior. such as elasto-plastic. The mechanics of particle shape change can be modeled over a range of complexity as shown in Figure 9.1(a)-(c). For elastic particles, single degree-of-freedom models describe each particle using its center of mass (Figure 9.1(a)) and mimic elastic shape changes through the form of the interaction potential with the system boundaries and other particles. The elastic contact between two particles that repel each other can be approximated by a Hertzian central force law that is a function of the interparticle overlap between the particles. ¹⁰ This approach can also be used to model adhesive contacts¹¹ and interactions between non-spherical elastic particles. 12 Level-set methods. 13,14 which use a signed distance function to determine interparticle separations, can be employed to calculate the interparticle potential energy and forces between pairs of arbitrarily shaped non-spherical particles. Even though level-set methods explicitly represent non-spherical particle shapes, they do not accurately model large particle shape deformation. Point-particle and level-set methods are computationally efficient, but they can accurately model particle deformation only for strains ≤10%. On the more complex end of the spectrum are volumetric meshes that accurately model the elastic energy of particle shape deformations, such as finite element methods (FEM) as illustrated in Figure 9.1(c). These methods can capture the changes in particle shape that arise from the propagation of stress through the volume of the particle that are generated from multiple contacts between the system boundaries and other particles. Volumetric meshes are computationally costly, and thus these methods have mainly been used to study packings of $\lesssim 10^3$ nearly spherical particles. ^{15–18}

The properties of many soft particulate systems, such as foams, ¹⁹ liquid bridges, ²⁰ and capillary droplets, ²¹ are governed by surface tension. In these systems, the shapes of the soft particles are obtained by finding the minimal surface area for a given particle energy, volume, or boundary condition. Particle shapes in these systems can be obtained using surface meshes (Figure 9.1(b)) and minimizing the total surface energy subject to the imposed constraints. ^{22–24}

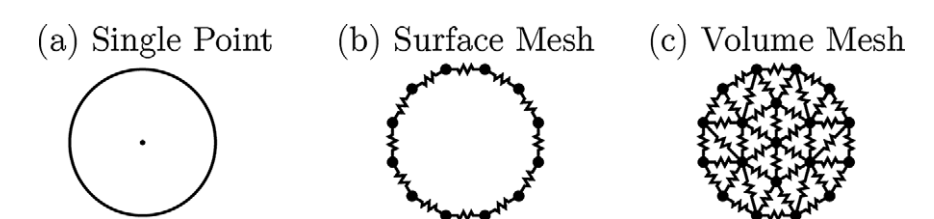


Figure 9.1 Methods to describe the mechanics of particle shape deformations: (a) a single degree of freedom located at the center of mass; (b) a surface mesh, where the number of degrees of freedom per particle scales as R^{d-1} , where R is the radius of the particle and d is the spatial dimension; and (c) a volumetric mesh, where the number of degrees of freedom per particle scales as R^d .

Given that surface meshes are more computationally efficient than volumetric meshes, it would be beneficial to develop effective surface energies and meshes that can describe the shape deformations of elastic particles. Surface meshes can also be used to describe plastic shape deformations, such as in clays²⁵ and polymeric materials under large stresses,²⁶ where the particle does not return to its initial shape after the applied stresses are removed.

In previous work, we developed the "deformable particle model" that describes particle shape changes using triangulated surface meshes and shape-energy functions that can describe elastic, surface-energy dominated, plastic, as well as elasto-plastic mechanics of particle shape deformation. Using the deformable particle model, we studied the jamming of underconstrained deformable particles in 2D²⁷ and 3D.²⁸ In addition, we carried out discrete element method simulations of the deformable particle model to study the mechanical properties of thin elastic shells,²⁹ elasto-plastic behavior in cell monolayers, ^{30,31} and flow and clogging of capillary droplets through narrow constrictions.³²

The remainder of the chapter is organized as follows. In Section 9.2, we highlight the variety of deformable particle systems that people interact with on a regular basis and those that are topics of current research. We also provide illustrations and simple explanations of the computational models of deformable particles and associated calculations that will be discussed in later sections. In Section 9.3, we describe the shape-energy functions in 2D and 3D that can be employed in the deformable particle model to simulate floppy particles that can change their shapes without energy cost, elastic shells, elastic solid particles, and capillary droplets. We also define the interactions between pairs of deformable particles and quantify the frictional forces between particles arising from smooth and rough interaction models. In Section 9.4, we describe calculations of the structural and mechanical properties of jammed packings of deformable particles, including the packing fraction and stress tensor in periodic boundary conditions and for shape-energy functions with many-body potentials. We also calculate the vibrational modes of jammed packings of deformable particles for several shape-energy functions, including elastic shells, capillary droplets, and floppy particles. We relate the scaling of the vibrational frequencies with the pressure to the number of contacts at jamming onset and the pressure-dependence of the shear modulus above jamming onset. Finally, in Section 9.5, we summarize the chapter and provide directions for future research, such as using the deformable particle model to describe tessellated granular systems with rigid and flexible boundaries for applications in soft robotics.

9.2 Deformable Particle Systems in Everyday Life

All of us frequently interact with deformable particles, including bowls of cooked rice and other foods, piles of rubber balls and other kids' toys, and emulsion-based lotions and consumer products. Deformable particles are also ubiquitous in science and engineering, for example, in studies of cell

and tissue mechanics, microfluidic devices, and elastic materials. We have developed a computational "deformable particle" model to better understand the single- and multi-particle properties of deformable particles. In this section, we introduce the main categories of deformable particles and give examples for each category. We also illustrate how the calculations in later sections provide insight into deformable particle systems.

There are several types of deformable particles. We will focus on four types in this work: floppy particles, like popping pearls in boba tea (Figure 9.2(a)), elastic shells like car tires (Figure 9.2(b)), particles whose shape is determined primarily through surface energy like soap bubbles (Figure 9.2(c)), and solid elastic particles like hydrogels used in hot and cold packs (Figure 9.2(d)) or bouncy ball kids' toys. Similar types of deformable particles occur in science and engineering and quantitatively accurate computational models are necessary to understand their properties (see Figure 9.2(a)–(d)).

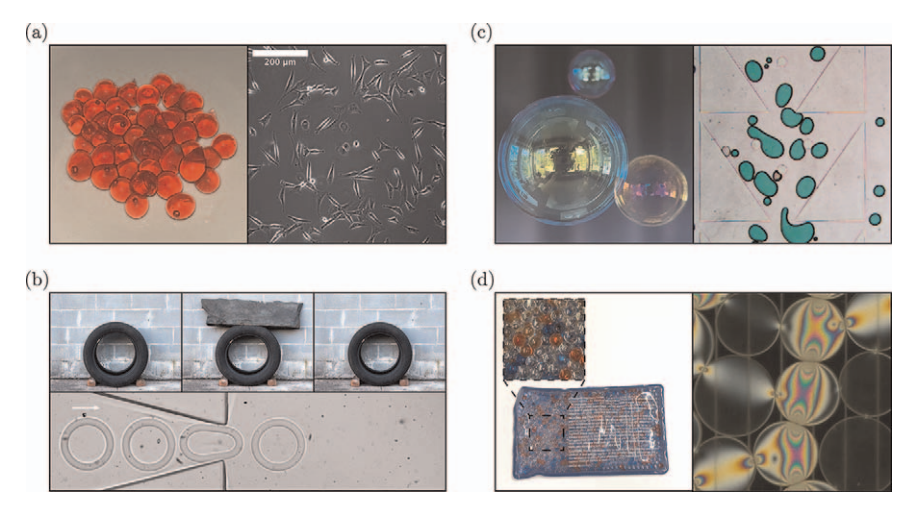


Figure 9.2 Examples of deformable particle systems. (a) Floppy particles: (left) popping boba pearls with diameter ~1 cm and (right) highly aspherical, ~50 µm long NIH3T3 cells on an untreated glass coverslip (credit: Yimin Luo). (b) Examples of elastic shells undergoing perturbations and returning to their original shapes: (top) a car tire, diameter ~0.5 m, compressed under a ~100 kg rock and (bottom) time series for diameter ~300 μm (bottom) cured polyethylene glycol diacrylate hydrogel shells that are driven through an orifice in a microfluidic channel, where the white arrow indicates the direction of the flow (credit: Amir Pahlavan). (c) Surface tension-dominated particles: (left) diameter \sim 5 cm soap bubbles in air and (right) \sim 300 μ m diameter water droplets (with green food coloring) in silicon oil flowing from top to bottom through polydimethyl-siloxane channels (credit: David J. Meer and Eric R. Weeks). (d) Elastic solid particles: (left) hot and cold pack filled with \sim 0.5 cm diameter hydrogel particles, where the inset shows a close up of the particles, and (right) ~5 cm diameter photoelastic particles under compression, where the fringe pattern shows the stress distribution.

Explicit modeling of particle shape change is also needed to calculate the forces arising from particle deformations, like the stresses visible in the photoelastic particles in Figure 9.2(d). For floppy particles, elastic shells, and surface energy-dominated particles, the stresses that arise from particle deformation can be described using a surface mesh as described in Section 9.3.1. For elastic solid particles, volumetric meshes are typically used to describe the stresses that arise from particle deformation. In this chapter, we introduce a surface-mesh approach that can be used to capture the mechanical response of elastic solid particles.

Different types of deformable particles possess varying particle interactions. For example, some deformable particles can slide past each other easily, while others can possess frictional and adhesive contact interactions. In Figure 9.3, we show how surface roughness can impact the collective mechanical properties of deformable particle systems flowing under the influence of gravity. When the deformable particles have rough surface interactions, the system remains a multilayered structure with a nonzero angle of repose even when the right wall is removed and the deformable particles are no longer confined (see Figure 9.3(a) and (b)). In contrast, when the deformable particles possess smooth interactions, they spread out over a much wider horizontal region (with a flat surface and zero angle of repose) when the right wall is removed as shown in Figure 9.3(c) and (d)). In Section 9.3.3, we calculate the effective friction coefficient between two interacting deformable particles and investigate how the effective friction coefficient changes with particle deformation.

When external stress is applied to a system of deformable particles, the particles can change in size and shape. In Figure 9.4(a), we show results from

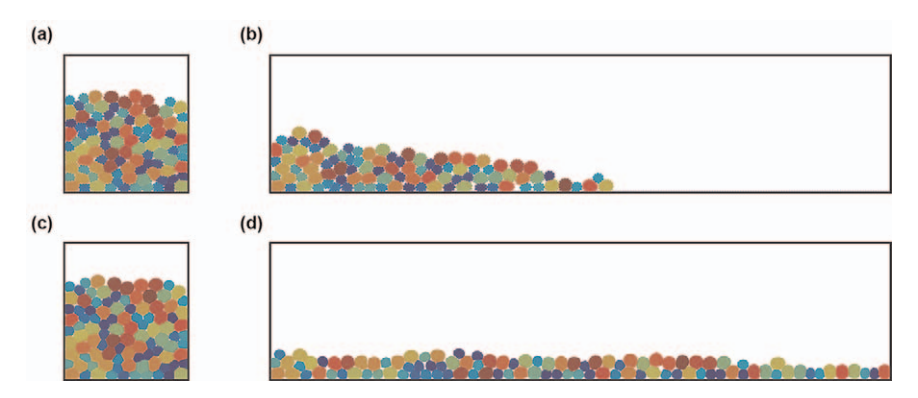


Figure 9.3 Slump tests for collections of deformable particles with different contact interactions. One hundred deformable particles with (a) rough and (c) smooth particle surfaces under the influence of gravity (in the downward direction) confined on the left and right by frictionless walls and on the bottom by a wall with a small friction coefficient. (b) and (d) The right wall is removed for the systems in (a) and (c) and the particles are allowed to run out and come to rest during damped molecular dynamics simulations.

simulations of a system of repulsive, "soft" disks (cf. Figure 9.1(a)) undergoing uniaxial compression. Allowing overlaps between soft particles is a common approximation for particle deformation. In Figure 9.4(b), we carry out simulations of a collection of deformable particles with the same bulk modulus as the "soft" disks undergoing the same uniaxial strain. We find clear differences between the two systems undergoing uniaxial compression, e.g. the deformable particles form facets at the interparticle contacts and the collection of deformable particles is confluent. In Sections 9.4.1 and 9.4.2, we provide the technical details to calculate the system's packing fraction, stress tensor, and pressure for collections of deformable particles.

In addition to the shear stress and pressure, another property that is used to characterize the collective response of particle packings is the density of vibrational modes. The vibrational modes provide a basis for collective motion and are characterized by a frequency ω and an energy cost that scales with ω^2 . Thus, the lowest energy collective particle motions possess the lowest frequencies. The vibrational modes are obtained by diagonalizing the dynamical matrix, which is the matrix of all possible second derivatives of the potential energy with respect to the particle positions (see Section 9.4.3). In Figure 9.5(a), we show that the vibrational modes are phonons in crystalline materials, which can be used to describe heat and electromagnetic transport in ordered solids. In contrast, disordered materials do not possess phonons. For example, in jammed packings of soft disks at low pressure, the low-frequency vibrational modes are quasi-localized, i.e. the particle displacements in these modes only involve a small fraction of the particles in the system (see Figure 9.5(b)). When explicit particle shape degrees of freedom are included, the modes are more complex and include particle translations, rotations, and deformations as shown in Figure 9.5(c) and (d). Investigating the vibrational modes is important for understanding the mechanical properties of deformable particle packings, such as how the

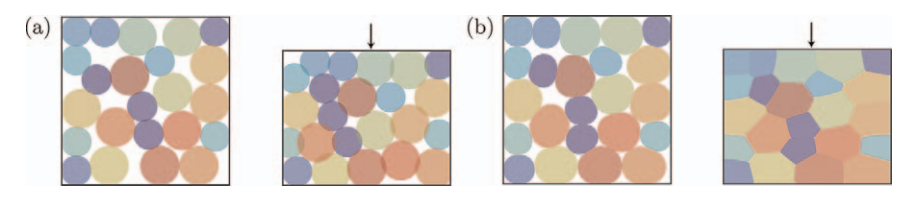


Figure 9.4 Collections of disks in 2D undergoing uniaxial compression in originally square boxes with repulsive walls. (a) (left) System of purely repulsive "soft" disks. (right) System in left panel is compressed by 20% in the direction of the arrow, which causes an increase in pressure and visible overlaps between particles. (b) (left) System of purely repulsive deformable particles at a similar pressure to that in the left panel of (a). (right) System in left panel is compressed by 20% in the direction of the arrow, which causes the particles to form facets at the contacts with no overlaps.

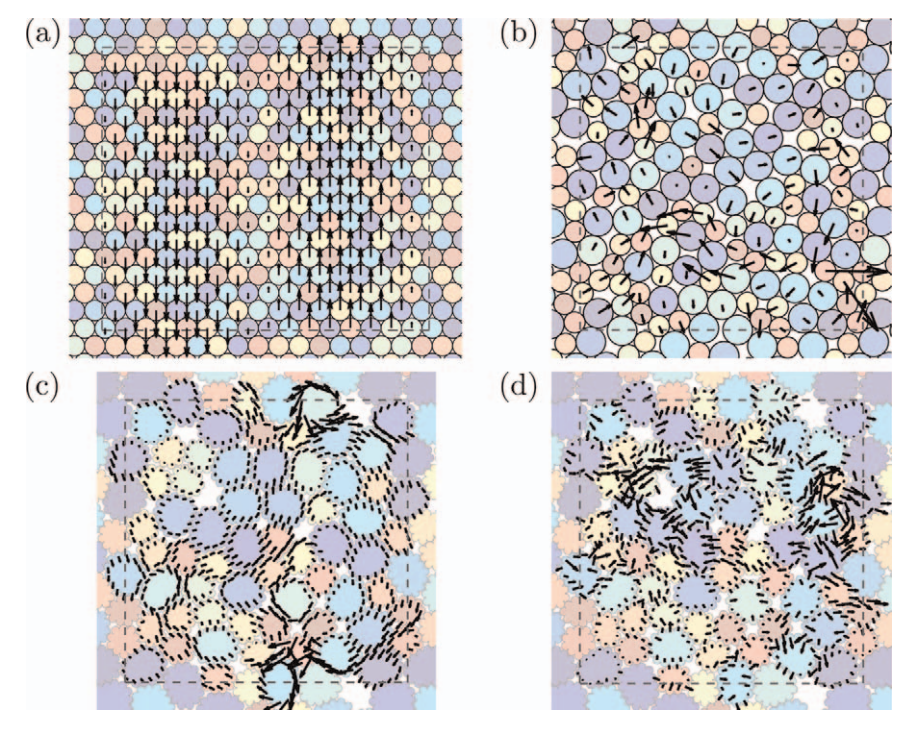


Figure 9.5 Visualizations of the vibrational modes for several particulate systems, where the black arrows indicate the particle displacements in a given mode. (a) A low-frequency phonon for a static packing of repulsive soft disks arranged on a hexagonal lattice. (b) The lowest frequency mode in a disordered, static soft disk packing at jamming onset. (c) A low-frequency, "quartic" mode and (d) a high-frequency, "quadratic" mode, in a "floppy" deformable particle packing.

shear modulus scales with pressure for different shape-energy functions (see Section 9.4.3).

9.3 Shape Mechanics for Deformable Particles

The deformable particle model describes the mechanics of deformable particles in 2D and 3D using surface meshes. The total potential energy for the deformable particle model includes a shape-energy function that determines the equilibrium shape for an individual deformable particle and an interaction potential that specifies the interparticle forces. In this section, we will define shape-energy functions that can describe the mechanics of elastic shells, surface-energy dominated particles, and elastic solids. We also define repulsive interactions between rough deformable particles and between smooth deformable particles in 2D, and calculate the effective friction coefficients in the two cases during simple shear tests.

9.3.1 Shape-energy Function

In 2D, the surface of particle μ can be described by a set of N_{μ} vertices that are connected by N_{μ} edges, forming a closed polygon, as shown in Figure 9.6(a). The mechanics of deformable particle μ in 2D is controlled by a shape-energy function $U_{\mu, \text{shape}}^{\text{2D}}$ that can be written in terms of the vertex positions:

$$U_{\mu,\text{shape}}^{\text{2D}} = \frac{k_{\text{a}}^{\text{2D}}}{2} (a_{\mu} - a_{\mu 0})^{2} + \sum_{i=1}^{N_{\mu}} \frac{k_{\text{l}}^{\text{2D}}}{2} (l_{\mu i} - l_{\mu i 0})^{2} + \sum_{i=1}^{N_{\mu}} \frac{k_{\text{b}}^{\text{2D}}}{2} (\theta_{\mu i} - \theta_{\mu i 0})^{2} + \gamma^{\text{2D}} p_{\mu},$$

$$(9.1)$$

where a_{μ} is the area of the particle μ , $l_{\mu i}$ is the length of edge i that lies between vertex i-1 and vertex i, and $\theta_{\mu i}$ is the bending angle between edges i-1 and i. (Vertices are indexed counter-clockwise around each particle.) The

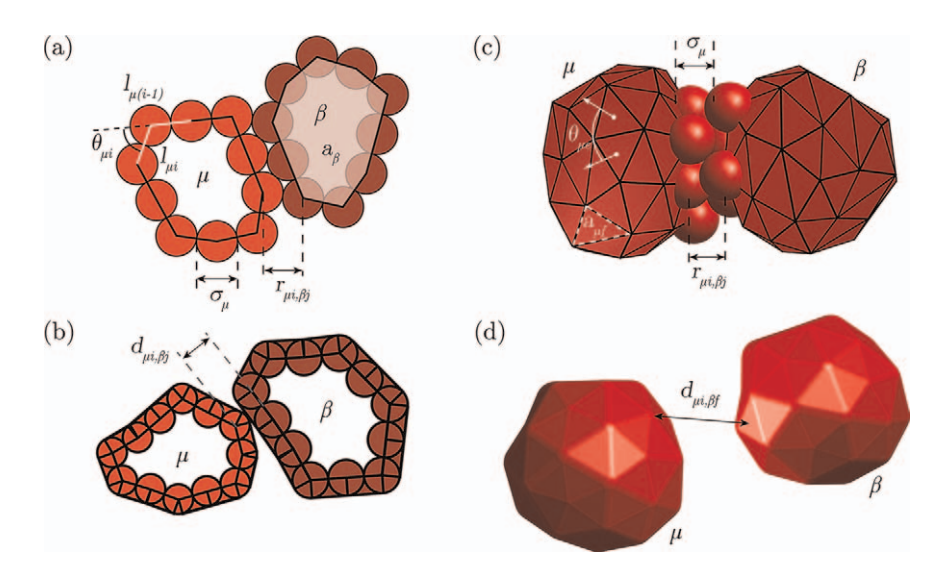


Figure 9.6 Images of the rough and smooth deformable particle models in 2D and 3D. (a) Two deformable particles μ and β with rough surfaces in 2D, where a_{β} is the polygonal area of particle β , $l_{\mu i}$ is the length of edge i, $\theta_{\mu i}$ is the bending angle between edge i and i-1, σ_{μ} is the diameter of each vertex on particle μ , and $r_{\mu i,\beta j}$ is the separation between vertex i on particle μ and vertex j and particle β . (b) Two deformable particles with smooth surfaces in 2D, where $d_{\mu i,\beta j}$ is the shortest distance between vertex i on particle μ to the line defined by edge i on particle β (see eqn (9.7)). (c) Two deformable particles with rough surfaces in 3D, where a_{uf} is the area of triangular face f on particle μ , $\theta_{\mu e}$ the bending angle for edge e on particle μ , σ_{μ} is the diameter of each vertex on particle μ , and $r_{\mu i,\beta j}$ is the separation between vertex i on particle μ and vertex j on particle β . Only a few spherical vertices are included on particles μ and β for visual clarity. (d) Two deformable particles with smooth surfaces in 3D, where $d_{\mu i,\beta f}$ is the shortest distance between vertex i on particle μ to the plane defined by face f on particle β .

first term in eqn (9.1) provides a quadratic energy penalty for deviations of the particle area from the preferred area $a_{\mu 0}$. The second term provides a quadratic energy penalty for deviations of the length of each edge from its preferred length $l_{\mu i0}$. The third term provides a quadratic energy penalty for deviations of each bending angle from its preferred angle $\theta_{\mu i0}$, which approximates the curvature energy. The parameters $k_{\rm a}^{\rm 2D}$, $k_{\rm l}^{\rm 2D}$, and $k_{\rm b}^{\rm 2D}$ control the magnitude of fluctuations in the area, edge length, and bending angle.

The perimeter of particle μ is given by $p_{\mu} = \sum_{i=1}^{N_{\mu}} l_{\mu i}$, and thus γ^{2D} in the fourth term in eqn (9.1) is the line tension that penalizes increases in perimeter.

The shape of each particle μ in 2D can be characterized using the "shape parameter," $\mathcal{A}^{\mathrm{2D}} = p_{\mu}^{\ 2}/(4\pi a_{\mu})$. The minimum value for the shape parameter is $\mathcal{A}_{\min}^{\mathrm{2D}} = N_{\mu} \tan(\pi/N_{\mu})/\pi$, which corresponds to a regular polygon, or a circle with $\mathcal{A}_{\min}^{\mathrm{2D}} = 1$ in the limit $N_{\mu} \rightarrow \infty$. For a shape-energy function with $k_{\mathrm{a}}^{\mathrm{2D}} > 0$, $k_{\mathrm{b}}^{\mathrm{2D}} > 0$, and $\gamma^{\mathrm{2D}} = 0$, in equilibrium, particle μ will possess

$$\mathcal{A}^{\mathrm{2D}} = \mathcal{A}_0^{\mathrm{2D}}$$
, where $\mathcal{A}_0^{\mathrm{2D}} = \left(\sum_{i=1}^{N_{\mu}} l_{\mu i 0}\right)^2/(4\pi a_{\mu 0})$. For a shape-energy function

with $k_a^{\rm 2D} > 0$ and $k_1^{\rm 2D} > 0$, either sufficiently large $\gamma^{\rm 2D}$ or $k_b^{\rm 2D}$ with $\theta_{\mu i0} = 0$ will drive the particle toward a circular shape with $\mathcal{A}^{\rm 2D} = \mathcal{A}_{\min}^{\rm 2D} < \mathcal{A}_0^{\rm 2D}$.

In three dimensions, we describe the surface of particle μ using a triangulated mesh with N_{μ} vertices, $N_{\mu f}$ triangular faces, and $N_{\mu e}$ edges between adjacent triangles that satisfy the Euler characteristic: $N_{\mu} + N_{\mu f} - N_{\mu e} = 2$ (see Figure 9.6(c)). Each surface triangle has three edges, each edge is shared by two triangles, and thus $2N_{\mu e} = 3N_{\mu f}$. When we combine this relation with the Euler characteristic, we obtain $N_{\mu f} = 2N_{\mu} - 4$ and $N_{\mu e} = 3N_{\mu} - 6$. The mechanics of deformable particle μ in 3D is controlled by a shape-energy function $U_{\mu, \text{shape}}^{3D}$ that can be written in terms of the vertex positions:

$$U_{\mu,\text{shape}}^{3D} = \frac{k_{\text{v}}^{3D}}{2} (\nu_{\mu} - \nu_{\mu 0})^2 + \sum_{f=1}^{N_{\text{uf}}} \frac{k_{\text{a}}^{3D}}{2} (a_{\mu f} - a_{\mu f 0})^2 + \sum_{e=1}^{N_{\mu e}} \frac{k_{\text{b}}^{3D}}{2} (\theta_{\mu e} - \theta_{\mu e 0})^2 + \gamma^{3D} s_{\mu},$$

$$(9.2)$$

where ν_{μ} is the volume of particle μ , $a_{\mu f}$ is the area of triangle f on particle μ , and $\theta_{\mu e}$ is the angle between two adjacent triangles that share edge e. The first term in eqn (9.2) is a quadratic energy penalty for deviations in the volume of particle μ from its preferred volume $\nu_{\mu 0}$. The second term is a quadratic energy penalty for deviations in the area of triangle f from its preferred area $a_{\mu f0}$. The third term is a quadratic energy penalty for deviations in the bending angle $\theta_{\mu e}$ from its preferred value $\theta_{\mu e0}$, which approximates the curvature energy. $\gamma^{\rm 3D}$ gives

the surface tension, where $s_{\mu} = \sum_{f=1}^{N_{\mu f}} a_{\mu f}$ is the total surface area of particle μ .

 $k_{\rm v}^{\rm 3D}$, $k_{\rm a}^{\rm 3D}$, and $k_{\rm b}^{\rm 3D}$ are parameters that control the magnitude of fluctuations in the volume, surface area, and bending angle, respectively.

In 3D, we characterize the shape of particle μ using the shape parameter $\mathcal{A}^{3D} = s_u^{3/2}/(6\sqrt{\pi}v_u)$. The lowest possible shape parameter corresponds to a sphere with $A^{3D} = 1$. However, in general, in 3D, the minimum shape parameter for a triangulated surface with N_{μ} vertices is not known. When N_{μ} is consistent with a surface mesh composed of equilateral triangles, such as Platonic solids with $N_{\mu} = 4$ (regular tetrahedron), 6 (regular octahedron), and 12 (regular icosahedron), we find $A_{\min}^{3D} = 1.8188$, 1.2861, and 1.0984. Thus, \mathcal{A}_{\min}^{3D} depends on N_{μ} and the placement of the vertices on the particle surface. The choice of N_{μ} is a compromise between having a sufficient number of vertices to describe fluctuations of the particle surface and computational cost. For many applications, we have employed deformable particle models with $N_{\mu} = 42$ arranged on a geodesic icosahedron with $\mathcal{A}_{\min}^{\mathrm{3D}} = 1.024.^{28,39}$ Even for structures that have $\mathcal{A}^{\mathrm{3D}} = \mathcal{A}_{\min}^{\mathrm{3D}}$ for a given N_{μ} , the preferred triangle areas $a_{\mu f0}$ and bending angles $\theta_{\mu e0}$ are not uniform over the surface. For a deformable particle with $k_v^{3D} > 0$, $k_a^{3D} > 0$, $k_b^{3D} = 0$, and $\gamma^{3D} = 0$, in equilibrium, particle μ will possess $\mathcal{A}^{\mathrm{3D}}=\mathcal{A}_0^{\mathrm{3D}}$, where $\mathcal{A}_0^{\mathrm{3D}}=\left(\sum_{f=1}^{N_{\mu f}}a_{\mu f0}\right)^{3/2}/(6\sqrt{\pi}\nu_{\mu 0})$. For a deformable particle with $k_{\rm v}^{\rm 3D}\!>\!0$ and $k_{\rm a}^{\rm 3D}\!>\!0$, either sufficiently large $\gamma^{\rm 3D}$ or $k_{\mathrm{b}}^{\mathrm{3D}}$ with $\theta_{\mu e0}\!=\!0$ will drive the particle toward a spherical shape with $A^{3D} = A^{3D}_{min}$.

Using the definitions of the shape-energy functions for deformable particles in 2D and 3D (eqn (9.1) and (9.2)), we can model a wide array of soft particulate materials by varying the parameters k_a^{2D} (k_v^{3D}), k_l^{2D} (k_a^{3D}), and γ^{2D} (γ^{3D}). In Table 9.1, we show that we can describe three types of deformable particles with different shape deformation mechanics. First, "floppy" particles with $k_a^{2D} > 0$ ($k_v^{3D} > 0$) and $k_l^{2D} > 0$ ($k_a^{3D} > 0$) can maintain their area (volume) and perimeter (surface), but the particles possess zero energy modes for transforming between shapes with the same shape parameter \mathcal{A}^{2D} (\mathcal{A}^{3D}) (see Section 9.4.3). In prior studies, we have

Table 9.1 Selections for the parameters, $k_{\rm a}^{\rm 2D}$ ($k_{\rm v}^{\rm 3D}$), $k_{\rm l}^{\rm 2D}$ ($k_{\rm a}^{\rm 3D}$), $k_{\rm b}^{\rm 2D}$ ($k_{\rm b}^{\rm 3D}$), and $\gamma^{\rm 2D}$ ($\gamma^{\rm 3D}$), in the shape-energy functions in 2D (eqn (9.1)) and 3D (eqn (9.2)) that describe "floppy" particles, elastic shells, and surface-energy dominated particles.

$k_{\rm a}^{ m 2D}\left(k_{ m v}^{ m 3D} ight)$	$k_{\mathrm{l}}^{\mathrm{2D}}\left(k_{\mathrm{a}}^{\mathrm{3D}}\right)$	$k_{\mathrm{b}}^{\mathrm{2D}}\left(k_{\mathrm{b}}^{\mathrm{3D}}\right)$	$\gamma^{2D}(\gamma^{3D})$	System description
>0	>0	0	0	Particles that conserve area (volume) and A , but possess floppy shapes, <i>e.g.</i> inflatable actuators ³³ and epithelial cells ³⁴
>0	>0	>0	0	Particles that maintain their shapes, <i>e.g.</i> elastic shells ³⁵ and platelets ³⁶
>0	≈0	0	>0	Particle shapes are controlled by line (surface) tension and are circular (spherical), <i>e.g.</i> capillary droplets ³⁷ and bubbles ³⁸

modeled cell monolayers $^{27-29}$ and cancer cells invading adipose tissue as floppy particles. 39 Second, for $k_{\rm a}^{\rm 2D} > 0$ ($k_{\rm v}^{\rm 3D} > 0$), $k_{\rm l}^{\rm 2D} > 0$ ($k_{\rm a}^{\rm 3D} > 0$), and $k_{\rm b}^{\rm 2D} > 0$ ($k_{\rm b}^{\rm 3D} > 0$), we can model elastic shells, which will return to their equilibrium shapes after applied deformations. For $k_{\rm a}^{\rm 2D} > 0$ ($k_{\rm v}^{\rm 3D} > 0$) and $\gamma^{\rm 2D} > 0$ ($\gamma^{\rm 3D} > 0$), we can describe particles whose shapes are determined by line (surface) tension with circular (spherical) shapes in the absence of applied stresses, such as capillary droplets. 32 We can also describe plastic particle shape mechanics by including equations of motion for the preferred geometrical properties of the particles, such as $a_{\mu 0}$ ($\nu_{\mu 0}$), $l_{\mu e 0}$ ($a_{\mu f 0}$), and $\theta_{\mu e 0}$. 30,31 We have described the development of mesophyll tissue in plant leaves 48 and wound closure in epithelial tissue 31 using an elastic shell shape-energy function with plastic deformation of the edge lengths and bending angles.

9.3.2 Interaction Potential Energy

Both the shape-energy function of individual deformable particles and the interactions between deformable particles determine their shape mechanics. In this chapter, we focus on pairwise, repulsive interactions between deformable particles that prevent them from overlapping. We consider two types of repulsive interactions: (1) "rough" interactions between a circular (spherical) vertex on one particle and a vertex on a neighboring particle (Figure 9.6(a) and (c)) and (2) "smooth" interactions between a circular vertex on one particle and edges on a neighboring particle in 2D (or between a spherical vertex on one particle and triangular faces on a neighboring particle in 3D) (Figure 9.6(b) and (d)).

The potential energy for interactions between N rough deformable particles in 2D and 3D is

$$U_{\text{int}}^{\text{rough}} = \frac{1}{2} \sum_{\mu=1}^{N} \sum_{i=1}^{N_{\mu}} \sum_{\substack{\beta=1\\\beta \neq \mu}}^{N_{\mu}} \sum_{j=1}^{N_{\beta}} U_{\mu i, \beta j}^{\text{rough}},$$
(9.3)

where vertex i is on particle μ with N_{μ} vertices and vertex j is on particle β with N_{β} vertices,

$$U_{\mu i,\beta j}^{\text{rough}} = \frac{k_{\text{c}}}{2} \left(\sigma_{\mu\beta} - r_{\mu i,\beta j} \right)^{2} \Theta(\sigma_{\mu\beta} - r_{\mu i,\beta j}), \tag{9.4}$$

and $r_{\mu i,\beta j}$ is the magnitude of the separation vector between vertices, $\vec{r}_{\mu i,\beta j} = \vec{r}_{\beta j} - \vec{r}_{\mu i}$. $\sigma_{\mu \beta} = (\sigma_{\mu} + \sigma_{\beta})/2$ is the average diameter of the vertices on particles μ and β , $\Theta(\cdot)$ is the Heaviside step function that ensures that $U_{\mu i,\beta j}^{\rm rough}$ is nonzero only for $r_{\mu i,\beta j} < \sigma_{\mu \beta}$, and $k_{\rm c}$ is the spring constant of the interaction (see Figures 9.6(a) and (c) and 9.7(a)).

The potential energy in eqn (9.3) and (9.4) considers repulsive interactions between vertex i on particle μ and vertex j on particle β , which mimics repulsive interactions between rough deformable particles (see Figure 9.7(a)) that give rise to torques between contacting deformable particles. How can we model repulsive interactions between *smooth* deformable particles?

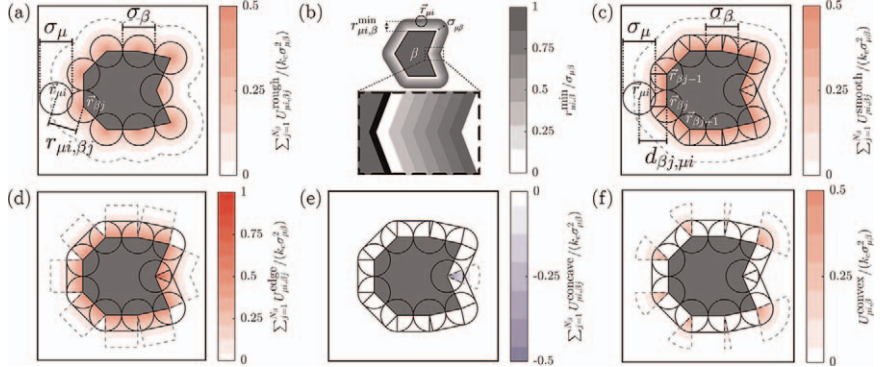


Figure 9.7 (a) The rough form for repulsive interactions between particles μ and β (eqn (9.3)). Vertex i on particle μ interacts with the vertices (labeled j) on particle β through the interaction potential, $\sum\limits_{j=1}^{N_{\beta}} U_{\mu i, \beta j}^{\mathrm{rough}}$ function of their separation $r_{\mu i,\beta j}$. Only one vertex i on particle μ is shown and $\sigma_{\mu\beta} = (\sigma_{\mu} + \sigma_{\beta})/2$ gives the range of the interaction. (b) The minimum distance $1 \le r_{\mu i,\beta}^{\min} / \sigma_{\mu\beta} \le 0$ between vertex i on particle μ and the edge of particle β with non-convex shape increases from white to dark gray. For non-convex shapes, the gradient of $r_{\mu\beta}^{\rm min}$ possesses discontinuities along lines that bisect concave angles of particle β . (c) The smooth interaction potential arising from vertex i interacting with particle β , $\sum_{i=1}^{i-\beta} U_{\mu i, \beta j}^{\mathrm{smooth}}$ where $U_{\mu i, \beta j}^{\mathrm{smooth}} = U_{\mu i, \beta j}^{\mathrm{edge}} + U_{\mu i, \beta j}^{\mathrm{concave}} + U_{\mu i, \beta j}^{\mathrm{convex}}$. (d)-(f) The contributions to the smooth interaction potential in (c) $U_{\mu i,\beta}^{\mathrm{edge}}, \sum_{j=1}^{N_{\beta}} U_{\mu i,\beta}^{\mathrm{concave}}, \text{ and } \sum_{j=1}^{N_{\beta}} U_{\mu i,\beta}^{\mathrm{convex}} \text{ separately. The discontinuity}$ in the concave region in the edge potential in (d) illustrates the need for the addition of $U_{\mu i,\beta j}^{\text{concave}}$ in $U_{\mu i,\beta j}^{\text{smooth}}$. In (a) and (c)-(f) when vertex i on particle μ is outside the dotted regions, its interaction with particle β is zero. We do not permit interactions between vertex i and particle β

A simple method for calculating the interaction energy between two smooth deformable particles is to assume that the pairwise potential energy for vertex i on particle μ interacting with particle β is a function of the minimum distance $r_{\mu i,\beta}^{\min}$ from vertex i to the nearest point on the closest edge (or face) of particle β . However, the gradient of $r_{\mu i,\beta}^{\min}$ is discontinuous along lines that bisect concave angles of particle β as shown in Figure 9.7(b), and thus the repulsive forces between particles μ and β would be discontinuous if we assumed this form for the smooth interaction potential.

when vertex i is in the dark-gray region.

We seek a smooth interaction potential that does not possess discontinuities in the repulsive forces between particles μ and β . To achieve this, we construct the smooth interaction potential $U_{\text{int}}^{\text{smooth}}$ that is a function of $r_{ui,\beta}^{\text{min}}$ when vertex i on particle μ interacts with a convex region of particle β ,

and gives rise to continuous forces when vertex i on particle μ interacts with concave regions of particle β (see Figure 9.7(c)). $U_{\rm int}^{\rm smooth}$ includes three terms. The first term is a function of the distance, $d_{\mu i, \beta j}$, from vertex i on particle μ to each overlapping edge j with width σ_{β} on particle β . In convex regions of particle β , vertex i can only overlap with one edge, while in concave regions vertex i can overlap with two or more edges (see Figure 9.7(d)). The second term is a function of the distance $r_{\mu i, \beta j}$ between vertex i on particle μ and overlapping vertex j on particle β , when j is in a concave region on particle β (see Figure 9.7(e)). Otherwise, the second term is zero. The third term is a function of the separation $r_{\mu i, \beta j}$ between vertex i on particle μ and vertex j on particle β when j is in a convex region and i and j overlap (see Figure 9.7(f)). The total potential energy $U_{\rm int}^{\rm smooth}$ arising from repulsive interactions between N smooth deformable particles in 2D is

$$U_{\text{int}}^{\text{smooth}} = \frac{1}{2} \sum_{\mu=1}^{N} \sum_{i=1}^{N_{\mu}} \sum_{\beta=1}^{N_{\mu}} \sum_{j=1}^{N_{\beta}} U_{\mu i, \beta j}^{\text{smooth}},$$
(9.5)

where μ and $\beta=1,\ldots,N$, $i=1,\ldots,N_{\mu}$, $j=1,\ldots,N_{\beta}$, and $U_{\mu i,\beta j}^{\rm smooth}=U_{\mu i,\beta j}^{\rm edge}+U_{\mu i,\beta j}^{\rm concave}+U_{\mu i,\beta j}^{\rm convex}$. The first term, $U_{\mu i,\beta j}^{\rm edge}$, includes repulsive spring interactions between vertex i on particle μ and edge j in convex and concave regions on particle β :

$$U_{\mu i,\beta j}^{\text{edge}} = \frac{k_{\text{c}}}{2} \left(\left(\sigma_{\mu\beta} - d_{\mu i,\beta j} \right)^{2} \Theta(\sigma_{\mu\beta} - d_{\mu i,\beta j}) \Theta(\vec{r}_{\beta(j-1),\mu i} \cdot \vec{r}_{\beta(j-1),\beta j}) \right.$$

$$\left. \cdot \Theta(\vec{r}_{\beta j,\mu i} \cdot \vec{r}_{\beta j,\beta(j-1)}) \Theta(d_{\mu i,\beta j}) \right), \tag{9.6}$$

where k_c is the spring constant. $d_{\mu i,\beta j}$ is the perpendicular distance between vertex i on particle μ and the line defined by edge j that runs from vertex $\vec{r}_{\beta(j-1)}$ to vertex $\vec{r}_{\beta j}$,

$$d_{\mu i,\beta j} = \hat{z} \cdot (\vec{r}_{\beta j,\beta(j-1)} \times \vec{r}_{\beta j,\mu i}) / |\vec{r}_{\beta j,\mu i}|, \tag{9.7}$$

where \hat{z} is a unit vector that is perpendicular to the 2D plane. The combined Heaviside functions in eqn (9.6) evaluate to 1 when vertex i is perpendicular to edge j and within the interaction range $\sigma_{\mu\beta}$ and evaluate 0 elsewhere.

When adjacent edges j-1 and j on particle β form a concave angle between 0 and $\pi/2$, a discontinuity occurs in $U^{\text{edge}}_{\mu i, \beta j}$. In particular, as vertex i on particle μ moves along edge j-1 on particle β , $U^{\text{edge}}_{\mu i, \beta j}$ jumps discontinuously when vertex i enters the portion of edge j that overlaps with edge j-1 (see Figure 9.7(d)). The second term, $U^{\text{concave}}_{\mu i, \beta j}$, removes this discontinuity.

$$U_{\mu i, \beta j}^{\text{concave}} = -\frac{k_c}{2} \left(\left(\sigma_{\mu \beta} - r_{\mu i, \beta j} \right)^2 \Theta(\sigma_{\mu \beta} - r_{\mu i, \beta j}) \Theta(\vec{r}_{\beta j, \mu i} \cdot \vec{r}_{\beta j, \beta (j-1)}) \right.$$

$$\left. \cdot \Theta(d_{\beta j, \mu i}) \Theta(\vec{r}_{\beta j, \mu i} \cdot \vec{r}_{\beta j, \beta (j+1)}) \Theta(d_{\beta (j+1), \mu i}) \right) \tag{9.8}$$

includes attractive interactions between vertex i on particle μ and vertex j on particle β that exactly cancel the discontinuous jump in $U_{\mu i, \beta j}^{\text{edge}}$. The combined Heaviside functions in eqn (9.8) evaluate to 1 when vertex i is within $\sigma_{\mu\beta}$ of

vertex j and within $\sigma_{\mu\beta}$ of both edges j and j+1. The third term $U_{\mu i,\beta j}^{\mathrm{convex}}$ captures the repulsive interactions between vertex i on particle μ and vertex j on particle β when vertex j lies between two edges that form a convex angle:

$$U_{\mu i, \beta j}^{\text{convex}} = \frac{k_{\text{c}}}{2} \left(\left(\sigma_{\mu \beta} - r_{\mu i, \beta j} \right)^{2} \Theta(r_{\mu i, \beta j} - \sigma_{\mu \beta}) \Theta(-\vec{r}_{\beta j, \mu i} \cdot \vec{r}_{\beta j, \beta (j-1)}) \Theta(-\vec{r}_{\beta j, \mu i} \cdot \vec{r}_{\beta j, \beta (j+1)}) \right). \tag{9.9}$$

The combined Heaviside functions in eqn (9.9) evaluate to 1 in the gaps between edges j and j+1 when they form a convex angle, when $r_{\mu i,\beta j} \leq \sigma_{\mu\beta}$, and evaluate to 0 otherwise (see Figure 9.3(f)).

9.3.3 Calculation of Friction Coefficient Between Deformable Particles During Simple Shear

After specifying the shape-energy function of deformable particles in Section 9.3.1 and repulsive interactions between them in Section 9.3.2, we will characterize their mechanical properties. In this section, we will calculate the effective friction coefficient between two deformable particles (both floppy particles and elastic shells with rough and smooth interactions) in 2D by carrying out a simple shear test, *i.e.* fixing the vertical separation between their centers and sliding them relative to each other in the horizontal direction. In the next section, we will characterize the normal force between two deformable particles in 2D and 3D by compressing them between two rigid flat plates.

We define the effective friction coefficient $\mu_{\rm eff}$ between two deformable particles μ and β undergoing simple shear as

$$\mu_{\text{eff}} = \frac{F_t}{F_n},\tag{9.10}$$

where

$$F_n = \vec{F}_{u\beta} \cdot \hat{n}_{\beta u}, \tag{9.11}$$

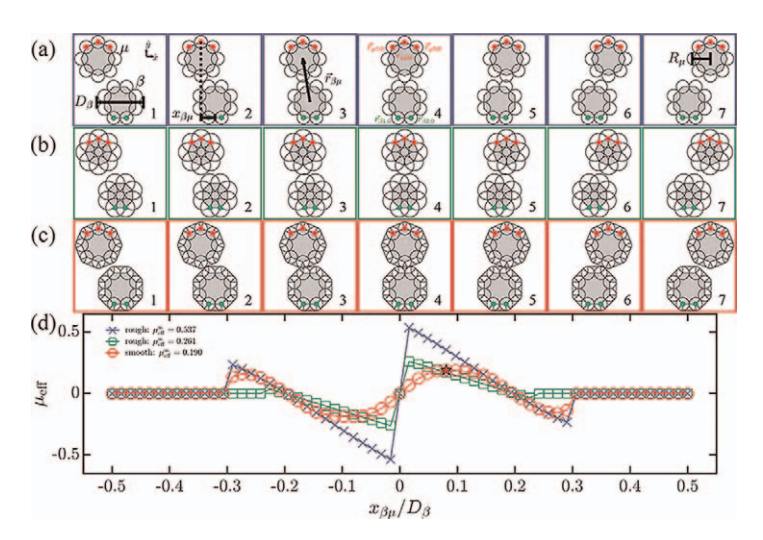
is the normal component of the force $\vec{F}_{\mu\beta} = -\sum\limits_{i=1}^{N_{\mu}} \vec{\nabla}_{\vec{r}_{\mu i}} U_{\mathrm{int}}^{\mathrm{smooth, rough}}$ on particle μ in the $\hat{n}_{\mu\beta}$ direction from interactions with particle β , $\hat{n}_{\beta\mu} = \vec{r}_{\beta\mu}/r_{\beta\mu}$ points from the center of mass of particle β to the center of mass of particle μ , and $\vec{\nabla}_{\vec{r}_{\mu i}}$ is the gradient with respect to the position of vertex i on particle μ . The tangential force component is

$$F_t = \vec{F}_{\mu\beta} \cdot \hat{t}_{\beta\mu},\tag{9.12}$$

where $\hat{t}_{\beta\mu}$ satisfies $\hat{n}_{\beta\mu} \times \hat{t}_{\beta\mu} = \hat{z}$.

To characterize the effective friction coefficient, we consider two deformable particles μ and β with eight vertices each $(N_{\mu} = N_{\beta} = 8)$ and identical shape and interaction potentials. The particles undergo simple shear by fixing the position of particle β and moving particle μ from left to right (see Figure 9.8(a)–(c)).

Fixing particle β and translating particle μ are achieved by adding harmonic spring potential energy functions. $U_{\beta}^{\text{constraint}} = \sum_{j=1}^{2} k_{\text{constraint}} |\vec{r}_{\beta j} - \vec{r}_{\beta j,0}|^2/2$ fixes the positions of the bottom two vertices 1 and 2 of particle β , $\vec{r}_{\beta 1}$ and $\vec{r}_{\beta 2}$, by defining "preferred" positions for each of them, $\vec{r}_{\beta 1,0}$ and $\vec{r}_{\beta 2,0}$. We use $U_{\mu}^{\text{constraint}} = \sum_{i=1}^{3} k_{\text{constraint}} |\vec{r}_{\mu i} - \vec{r}_{\mu i,0}|^2/2$ to shift the positions of vertices 1, 2, and 3 on particle μ , $\vec{r}_{\mu i}$ with i=1,2,3 from left to right, by incrementally changing the "preferred" positions $\vec{r}'_{\mu i,0} = \vec{r}_{\mu i,0} + \Delta x \hat{x}$, where $\Delta x = 0.016 D_{\beta}$ and $D_{\beta} = \max_{ij} |\hat{x} \cdot \vec{r}_{\beta i,\beta j}| + \sigma_{\beta}$ is the horizontal width of particle β . After each horizontal shift of particle μ , we relax the total potential energy of the system (including $U_{\mu,\text{shape}}^{\text{2D}}$, $U_{\beta,\text{shape}}^{\text{2D}}$, $U_{\text{int}}^{\text{rough}}$ or $U_{\text{int}}^{\text{smooth}}$, $U_{\mu}^{\text{constraint}}$, and $U_{\beta}^{\text{constraint}}$) using damped molecular dynamics simulations until the total kinetic energy, K,



Two elastic shell particles μ and β with $N_{\mu} = N_{\beta} = 8$ and $\mathcal{A}_{0}^{\text{2D}} = \mathcal{A}_{\min}^{\text{2D}}$ Figure 9.8 undergo simple shear by fixing the position of particle β and moving particle μ from left to right, which is achieved by adding two harmonic spring potential energy functions that prescribe the equilibrium positions $\vec{r}_{\beta 1,0}$ and $\vec{r}_{\beta 2,0}$ of two vertices (green) on particle β and the equilibrium positions $\vec{r}_{\mu 1,0}$, $\vec{r}_{\mu 2,0}$, and $\vec{r}_{\mu 3,0}$ of three vertices (red) on particle μ . $\vec{r}_{\beta\mu}$ is the separation vector from particle β to μ , D_{β} is the horizontal width of particle β , and R_{μ} is the distance from the center of particle μ to each vertex when particle μ is a regular polygon. Particle positions (varying in frames 1-7) for two particles of varying types undergoing simple shear as a function of $x_{\beta\mu} = \hat{x} \cdot (\vec{r}_{\mu 2,0} - (\vec{r}_{\beta 1,0} + \vec{r}_{\beta 2,0})/2)$: (a) two rough elastic shells with $C_{\mu} = R_{\mu}/\sigma_{\mu} = 1.3$ and $\mu_{\rm eff}^{\rm m} = 0.537$; (b) two rough elastic shells with $R_{\mu}/\sigma_{\mu}=0.71$ and $\mu_{\rm eff}^{\rm m}=0.261$; and (c) two smooth elastic shells with $C_{\mu}=R_{\mu}/\sigma_{\mu}=1.3$ and $\mu_{\rm eff}^{\rm m}=0.190$. (d) The effective coefficient of friction $\mu_{\rm eff}$ plotted *versus* $x_{\beta\mu}/D_{\beta}$ for the particle types in (a)–(c). The configuration at which the maximum effective friction coefficient $\mu_{\mathrm{eff}}^{\mathrm{m}}$ occurs for two smooth elastic shells is marked with a star.

satisfies $K/(k_c\sigma^2) \lesssim 10^{-20}$, where σ is the average vertex diameter. To ensure that the constrained vertices remain near their "preferred" positions, we chose $k_{\rm constraint}/k_c = 100$.

We first calculate $\mu_{\rm eff}(x_{\beta\mu})$, where $x_{\beta\mu}=\hat{x}\cdot(\vec{r}_{\mu2,0}-(\vec{r}_{\beta1,0}+\vec{r}_{\beta2,0})/2)$, for stiff, elastic shells $(k_{\rm l}^{\rm 2D}/k_{\rm c}=100,k_{\rm b}^{\rm 2D}/(k_{\rm c}\sigma^2)=171$, and $k_{\rm a}^{\rm 2D}a_0^2/(k_{\rm c}\sigma^2)=14$, where a_0 is the average preferred area) with rough interactions, $N_\mu=8$, and $\mathcal{A}_0^{\rm 2D}=\mathcal{A}_{\rm min}^{\rm 2D}$ (see Figure 9.8(a) and (b)). As the two particles are sheared, $\mu_{\rm eff}$ displays a "saw-tooth" pattern as the particles "stick" and "slip" past one another, ⁴⁰ as shown in Figure 9.8(d). $\mu_{\rm eff}$ starts at a small positive value at the first contact between the particles and decreases approximately linearly until it reaches its minimum value near $x_{\beta\mu}=0$. At $x_{\beta\mu}=0$, where one vertex on particle μ contacts two vertices on particle μ and fits into the groove between them, the particles only exert normal forces on each another and $\mu_{\rm eff}=0$ (see frame 4 in Figure 9.8(a)). For $x_{\beta\mu}\gtrsim 0$, one of these contacts breaks and $\mu_{\rm eff}$ jumps to its maximum value $\mu_{\rm eff}^{\rm m}=\max_{x_{\beta\mu}}\mu_{\rm eff}(x_{\beta\mu})$. $\mu_{\rm eff}$ then decreases roughly linearly as particle μ moves out of the groove of particle μ . At sufficiently large μ in Figure 9.8(a), the particles are no longer in contact (see frames 6 and 7 in Figure 9.8(a)).

Given the shapes, positions, and orientations of particles μ and β , $\mu_{\rm eff}$ for each two-particle configuration can be calculated, and the maximum value of $\mu_{\rm eff}(x_{\beta\mu})$ over all sampled configurations can be obtained. In the case of rough, circular particles with $\mathcal{A}_0^{\rm 2D} = \mathcal{A}_{\rm min}^{\rm 2D}$, the maximum effective friction coefficient is determined by the ratio of the polygon radius to the vertex diameter $C_\mu = R_\mu/\sigma_\mu$ and number of the vertices N_μ :⁴¹

$$\mu_{\text{eff}}^{\text{max}} = \left(\left[\frac{1}{C_{\mu} \sin \left(\pi / N_{\mu} \right)} \right]^{2} - 1 \right)^{-\frac{1}{2}}.$$
(9.13)

In Figure 9.8(a) and (b), we fix N_{μ} and R_{μ} and vary σ_{μ} to achieve $\mu_{\rm eff}^{\rm max}=0.577$ with $C_{\mu}=1.3$ and $\mu_{\rm eff}^{\rm max}=0.283$ with $C_{\mu}=0.71$. These calculated values of $\mu_{\rm eff}^{\rm max}$ are consistent with $\mu_{\rm eff}^{\rm m}=0.537$ and 0.261 that are found in Figure 9.8(d).

We then calculate μ_{eff} for stiff, elastic shells for smooth interactions with the same shape-energy function, $\mathcal{A}_0^{\text{2D}}$, and $C_\mu = 1.3$ as those for the rough, elastic shells in Figure 9.8(a). Unlike $\mu_{\text{eff}}(x_{\beta\mu})$ for rough interactions, μ_{eff} for smooth elastic shells does not possess large jumps while the particles are in contact as shown in Figure 9.8(d). Rather μ_{eff} begins at a small positive value and undergoes smooth oscillations between positive and negative values as $x_{\beta\mu}$ increases. As shown in frame 4 in Figure 9.8(c), when $x_{\beta\mu} = 0$, the dominant force between particles μ and β arises from overlaps between the bottom vertex of μ and the top edge of β and points in the $\hat{n}_{\beta\mu}$ direction, which is vertical in this configuration. Here, any tangential forces arising from interactions between the top two vertices of β and the bottom two edges of μ cancel. When $x_{\beta\mu} \gtrsim 0$, the dominant force on particle μ from β continues to point in the vertical direction, unlike rough interactions where for $x_{\beta\mu} \gtrsim 0$, $\vec{F}_{\mu\beta}$ has a large horizontal component. The maximum value of $\mu_{
m eff}^{
m m} = 0.190$ occurs when $x_{\beta\mu}/D_{\beta} \approx 0.1$, which is consistent with $\mu_{\rm eff}^{\rm max} = 0.190$ calculated for smooth, elastic shell particles in the configuration indicated by the star in

Figure 9.8(c). (See Appendix A for the calculation of $\mu_{\rm eff}^{\rm max}$ for smooth deformable particles.)

We now characterize the impact of particle deformability on μ_{eff} by calculating $\mu_{\text{eff}}(x_{\beta\mu})$ for floppy particles $(k_l^{\text{2D}}/k_c=1, k_b^{\text{2D}}=0, \text{ and } k_a^{\text{2D}}a_0^2/(k_c\sigma^2)=14)$ with rough and smooth interactions (see Figure 9.9(a)). We have additional control of the deformability by varying $A_0^{\rm 2D} = A_{\rm min}^{\rm 2D} \approx 1.05$, 1.15, and 1.3. $\mu_{\rm eff}$ for rough, floppy particles with $A_0^{\rm 2D} = A_{\rm min}^{\rm 2D}$ (Figure 9.9(b)) is similar to $\mu_{\rm eff}$ for rough, stiff elastic shells (Figure 9.8(d)), i.e., both possess saw-tooth patterns and similar $\mu_{\text{eff}}(x_{\beta\mu})$. For floppy particles with $\mathcal{A}_0^{\text{2D}} > \mathcal{A}_{\min}^{\text{2D}}$, $\mu_{\text{eff}}(x_{\beta\mu})$ changes dramatically. For $\mathcal{A}_{0}^{\mathrm{2D}}=$ 1.15, μ_{eff} is no longer symmetric as particle μ moves past particle β . Rather, $\mu_{\rm eff}(x_{\beta\mu})$ is irregular, it has a large region $-0.08 \lesssim x_{\beta\mu}/D_{\beta} \lesssim 0.4$ where $\mu_{\rm eff} \sim \mu_{\rm eff}^{\rm max}$ for rough, elastic shells. $\mu_{\rm eff} \sim \mu_{\rm eff}^{\rm max}$ occurs when the vertices of particle μ are located in the grooves of particle β and vice-versa. The deformability of the particles allows interdigitated configurations to occur over a wide range of $x_{\beta\mu}$ rather than at a single $x_{\beta\mu}$ as for rigid, elastic shells. For extremely floppy particles, such as $A_0^{2D} = 1.3$, the particles can explore elongated shapes, which can achieve larger friction coefficients than those that are possible for rough, nearly spherical elastic shells (see frame 6 in Figure 9.9(a)). We note that for floppy particles, the particle shape and effective friction coefficient are historydependent, and thus μ_{eff} would be different for a cyclic simple shear protocol.

Finally, we calculate $\mu_{\rm eff}$ for floppy particles with smooth interactions and the same shape-energy function that was used for the rough interactions (see Figure 9.9(c)). As before, $\mu_{\rm eff}$ for smooth particles with $\mathcal{A}_0^{\rm 2D}=\mathcal{A}_{\rm min}^{\rm 2D}$ is similar to that for smooth, elastic shells (see Figure 9.9(d)). $\mu_{\rm eff}$ for smooth, floppy particles with $\mathcal{A}_0^{\rm 2D}=1.15$ and 1.30 depend strongly on the shape of the particles. We find that smooth, floppy particles with $\mathcal{A}_0^{\rm 2D}=1.15$ possess the lowest $\mu_{\rm eff}^{\rm max}$ across all systems we considered, indicating a combination of deformability and surface interactions can lead to the least friction between particles undergoing simple shear. However, $\mu_{\rm eff}^{\rm max}$ for smooth, floppy particles with $\mathcal{A}_0^{\rm 2D}=1.30$ exceeds $\mu_{\rm eff}^{\rm max}$ for smooth, elastic shells. Thus, increasing deformability by increasing $\mathcal{A}_0^{\rm 2D}$ gives rise to non-monotonic behavior in $\mu_{\rm eff}^{\rm max}$. Together these results confirm the sensitivity of frictional interactions between deformable particles on the specific two-particle configurations that are sampled.

9.3.4 Contact Mechanics

In this section, we characterize the mechanical properties of individual deformable particles undergoing uniaxial compression. In particular, we compare the relation between the applied force and particle deformation for rough, elastic shells (with $\mathcal{A}_0^{\text{2D,3D}} = \mathcal{A}_{\min}^{\text{2D,3D}}$) and bulk elastic particles in 2D and 3D. We will confine a single deformable particle between two flat rigid parallel plates and determine the applied force F_a normal to the top plate that achieves a given compression distance δ (see Figures 9.10(a), (b) and 9.11(a)–(c)). We fix the bottom plate and move the top plate downward in small compression steps, with each followed by minimization of the total potential energy

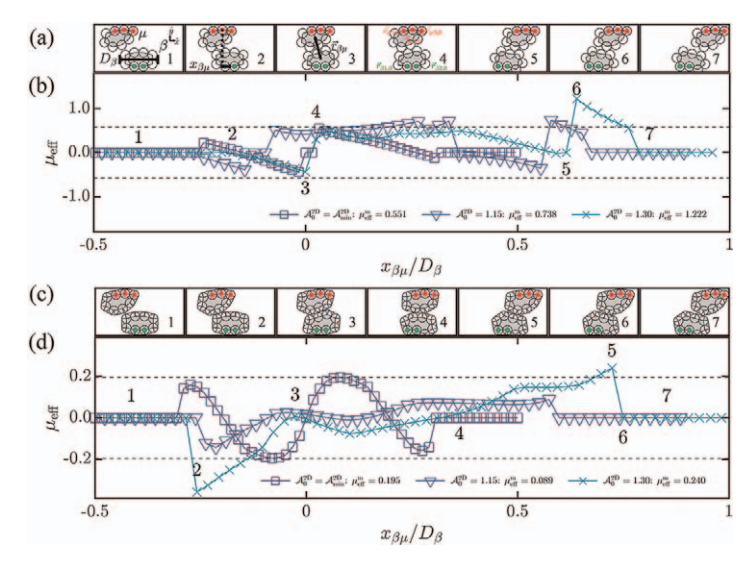


Figure 9.9 Two floppy particles μ and β with $N_{\mu} = N_{\beta} = 8$ undergoing simple shear by fixing the position of particle β and moving particle μ from left to right. This protocol is achieved by adding two harmonic spring potential energy functions that prescribe the equilibrium positions $\vec{r}_{\beta 1,0}$ and $\vec{r}_{\beta 2,0}$ of two vertices (green) on particle β and the equilibrium positions $\vec{r}_{\mu 1,0}$, $\vec{r}_{\mu 2,0}$, and $\vec{r}_{\mu 3,0}$ of three vertices (red) on particle μ . $\vec{r}_{\beta \mu}$ is the separation vector from particle β to μ , and D_{β} is the horizontal width of particle β . (a) Floppy, rough and (c) floppy, smooth (with $A_0^{2D} = 1.3$) particle shapes and positions (varying in frames 1–7) as a function of $x_{\beta \mu} = \hat{x} \cdot (\vec{r}_{\mu 2,0} - (\vec{r}_{\beta 1,0} + \vec{r}_{\beta 2,0})/2)$. $\mu_{\rm eff}$ plotted *versus* $x_{\beta \mu}/D_{\beta}$ for (b) floppy, rough and (d) floppy smooth particles with $A_0^{2D} = A_{\rm min}^{2D}$, 1.15, and 1.3. The horizontal dashed lines in (b) and (c) indicate $\pm \mu_{\rm eff}^{\rm max} = 0.577$ and 0.190 for elastic shell particles with rough and smooth interaction potentials, respectively, obtained from eqn (9.13) and Appendix A.

including the shape-energy function and repulsive interaction energy between vertices i on particle μ and the top (t=1) and bottom plates (t=2):

$$U_{\mu}^{
m plate} = \sum_{t=1}^{2} \sum_{i=1}^{N_{\mu}} \frac{k_{
m p}}{2} \left(\sigma_{\mu}/2 - r_{\mu i}^{
m plate,t} \right)^{2} \Theta\left(\sigma_{\mu}/2 - r_{\mu i}^{
m plate,t} \right), \text{ where } k_{
m p}/k_{
m c} = 4 \text{ is the }$$

spring constant for the plate-vertex interaction and $r_{\mu i}^{\text{plate},t}$ is the minimum distance between vertex i and plate t. These compression tests are similar to those used to quantify F_{a} versus δ for bulk elastic particles, such as compressing elastic cylinders in the radial direction in 2D and compressing elastic spheres in 3D.

In 2D, for an elastic cylinder with length l and diameter D parallel to and in contact with a plane of the same material, the applied force $F_{\rm a}$ to achieve compression δ is 42

$$\frac{\delta}{D} = \frac{4}{\pi} \frac{F_{\rm a}}{ED^2} \frac{D(1 - \nu^2)}{l} \left(1 + \ln \left[\frac{\pi l^3 ED^2}{(1 - \nu^2)D^3 F_{\rm a}} \right] \right), \tag{9.14}$$

where ν is the Poisson's ratio and E is the Young's modulus of the particle.

In dimensionless form, eqn (9.14) becomes
$$\tilde{\delta} = [4\tilde{F}_a \tilde{D}/\pi] \left(1 + \ln\left[\frac{\pi}{\tilde{D}^3 \tilde{F}_a}\right]\right)$$
,

where $\tilde{D}=D/l$, $\tilde{\delta}=\delta/D$, and $\tilde{F}_a=F_a(1-\nu^2)/(ED^2)$. In the small compression limit $\tilde{\delta}\ll 1$, eqn (9.14) can be approximated by a linear force–displacement relation: $\tilde{F}_a\propto\tilde{\delta}^a$ with $\alpha=1$. We find a similar result, $\tilde{F}_a\sim\tilde{\delta}$, when we compress an elastic solid disk modeled using a spring network (Figure 9.10(a)). The spring network is composed of a disordered triangular lattice with 1100 nodes connected by 3197 linear springs (for an average coordination number of 5.81) all with the same spring constant $k/k_c=1$. For compression of an elastic shell, we consider $\mathcal{A}_0^{\rm 2D}=\mathcal{A}_{\min}^{\rm 2D}$, $k_a^{\rm 2D}>0$, $k_b^{\rm 2D}>0$, $k_b^{\rm 2D}>0$, $\theta_{\mu i0}=2\pi/N_\mu$ for all i, and $N_\mu=100$ (Figure 9.10(b)). We also find that $\tilde{F}_a\propto\tilde{\delta}$ for compression of elastic shells using the deformable particle model for small $\tilde{\delta}$, while \tilde{F}_a increases nonlinearly for $\tilde{F}_a\gtrsim 10^{-2}$ as shown in Figure 9.10(c). Thus, for small deformations, both elastic shells and bulk elastic particles possess linear force–displacement relations during compression in 2D.

In 3D, $\tilde{F}_a = \frac{4}{3}\tilde{\delta}^{\alpha}$ with $\alpha = 1.5$ for an elastic solid sphere⁴² and $\tilde{F}_a \propto \tilde{\delta}$ for an elastic spherical shell.⁴³ When we model an elastic solid sphere as a volumetric spring network with 3765 nodes connected by 43, 334 springs with spring constant $k/k_c = 1$ and coordination number ≈ 23 (Figure 9.11(a)), we also find

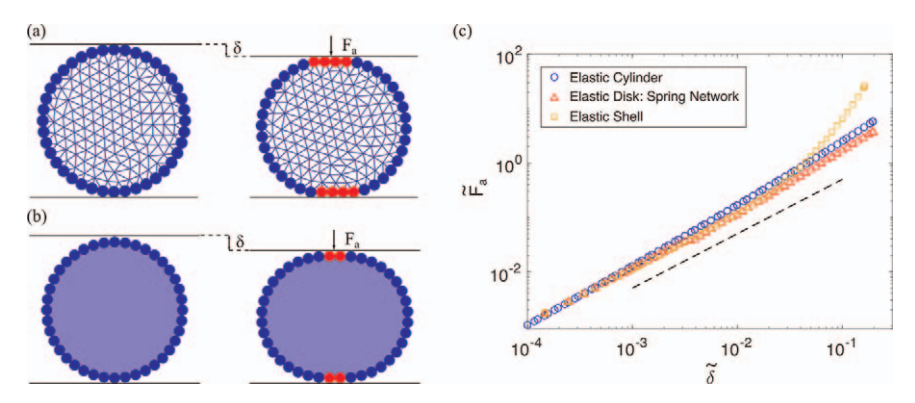


Figure 9.10 Images from compression tests in 2D for (a) an elastic disk modeled using a spring network with coordination number 5.81 that fills the entire disk and (b) an elastic shell with $\mathcal{A}_0^{2D} = \mathcal{A}_{\min}^{2D}$, $k_a^{2D} > 0$, $k_l^{2D} > 0$, and $\theta_{\mu i0} = 2\pi/N_{\mu}$ for all i. In (a) and (b), the red vertices are in contact with the top and bottom plates, δ and F_a define the compression distance and applied compression force, respectively. (Note that we do not show all of the vertices, nodes, and spring connections for visual clarity.) (c) Dimensionless applied force \tilde{F}_a plotted as a function of the dimensionless compression distance $\tilde{\delta}$ for an elastic cylinder (blue circles, eqn (9.14)), elastic disk modeled using a spring network (red triangles), and elastic shell (yellow squares). The dashed line has slope 1.

 $\tilde{F}_a \sim \tilde{\delta}^{\alpha}$ with $\alpha = 1.5$. For an elastic shell with $\mathcal{A}_0^{\rm 3D} = \mathcal{A}_{\rm min}^{\rm 3D}$, $k_{\rm v}^{\rm 3D} > 0$, $k_{\rm a}^{\rm 3D} > 0$, $k_{\rm b}^{\rm 3D} > 0$, and $\theta_{\mu e0}$ that correspond to the equilibrium bending angles for a polyhedron with $\mathcal{A}_0^{\rm 3D} = \mathcal{A}_{\rm min}^{\rm 3D}$ for $N_{\mu} = 162$ (Figure 9.11(b)), we find that $\tilde{F}_a \propto \tilde{\delta}$ over a large range of $\tilde{\delta}$ as found for the continuum description of an elastic spherical shell (see Figure 9.11(d)).

Can we develop a surface tessellation model that mimics the compressive response of an elastic solid sphere? We propose a model with a spherical surface tessellation (with N_{μ} vertices) plus an additional vertex at the particle's center that form $2N_{\mu}-4$ tetrahedra between the central vertex and triangles on the particle surface (Figure 9.11(c)). Instead of using $U_{\mu,\text{shape}}^{\text{3D}}$ in eqn (9.2), we assume that the following strain energy governs particle deformation during compression:

$$U_{\mu,\text{strain}}^{\text{3D}} = \sum_{f=1}^{2N_{\mu}-4} \sum_{m,n,q,r=1}^{3} \frac{v_f}{2} \varepsilon_{f,mn} C_{mnqr} \varepsilon_{f,qr}, \qquad (9.15)$$

where v_f is the volume of tetrahedron f, $\varepsilon_{f,mn}$ and $\varepsilon_{f,qr}$ are the components of the strain tensor ε_f for tetrahedron f, and C_{mnqr} is the elasticity tensor.

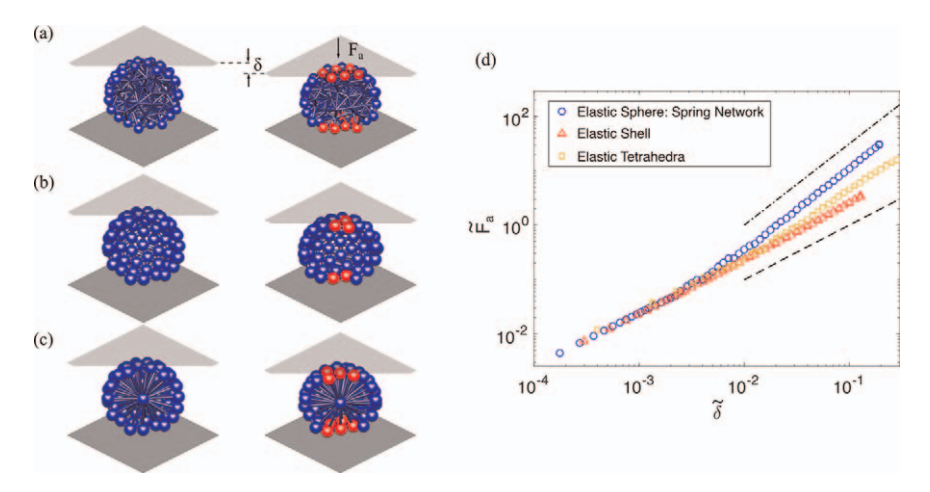


Figure 9.11 Images from compression tests in 3D for (a) an elastic sphere modeled by a volumetric spring network with coordination number \approx 23, (b) an elastic spherical shell with $\mathcal{A}_0^{\mathrm{3D}} = \mathcal{A}_{\min}^{\mathrm{3D}}$, $k_a^{\mathrm{3D}} > 0$, $k_a^{\mathrm{3D}} > 0$, $k_a^{\mathrm{3D}} > 0$, and $\theta_{\mu e0}$ that correspond to the equilibrium bending angles for a polyhedron with $\mathcal{A}_0^{\mathrm{3D}} = \mathcal{A}_{\min}^{\mathrm{3D}}$ for $N_{\mu} = 162$, and (c) $2N_{\mu} - 4$ elastic tetrahedra that are formed by the center of mass of the particle and the triangles that form its surface mesh. In (a)–(c), the red vertices indicate those in contact with the top and bottom plates. (Note that we do not show all of the vertices, nodes, and spring connections for visual clarity.) (d) Dimensionless applied force, \tilde{F}_a plotted as a function of dimensionless compression distance $\tilde{\delta}$ for an elastic shell (red triangles), spring network (blue circles), and elastic tetrahedra (yellow squares). The dashed and dash-dotted lines have slopes 1 and 1.5, respectively.

The strain tensor ε_f is given by the deformation tensor J_f of tetrahedron f: $\varepsilon_f = \left(J_f^T J_f - I\right)/2$, where I is the identity matrix. The deformation gradient tensor obeys $J_f = Y_f X_f^T (X_f X_f^T)^{-1}$, where X_f^T is the transpose of X_f , and X_f and Y_f are matrices formed from the separation vectors from the central vertex to the vertices of each surface triangle before and after deformation:

$$X_{f} = \left(\vec{r}_{f,1}^{0} - \vec{r}_{N_{\mu}+1}^{0}, \ \vec{r}_{f,2}^{0} - \vec{r}_{N_{\mu}+1}^{0}, \ \vec{r}_{f,3}^{0} - \vec{r}_{N_{\mu}+1}^{0}\right), \tag{9.16}$$

$$Y_f = (\vec{r}_{f,1} - \vec{r}_{N_u+1}, \ \vec{r}_{f,2} - \vec{r}_{N_u+1}, \ \vec{r}_{f,3} - \vec{r}_{N_u+1}), \tag{9.17}$$

where $\vec{r}_{f,1}^0$, $\vec{r}_{f,2}^0$, and $\vec{r}_{f,3}^0$ are the column vectors giving the coordinates of the three vertices that form surface triangle f before deformation, $\vec{r}_{f,1}$, $\vec{r}_{f,2}$, and $\vec{r}_{f,3}$ are the column vectors giving the coordinates of the three vertices that form the surface triangle f after deformation, and $\vec{r}_{N_{\mu}+1}^0$ and $\vec{r}_{N_{\mu}+1}$ are the column vectors giving the coordinates of the central vertex before and after deformation. When we assume that each tetrahedron is composed of the same isotropic elastic material, we find that $\tilde{F}_a \propto \tilde{\delta}^\alpha$ with $\alpha = 1.5$ during compression for sufficiently large displacements as shown in Figure 9.11(d). Note that for this model $\alpha \approx 1$ for small $\tilde{\delta}$ since at small deformations the purely repulsive linear spring forces between the surface vertices and the flat plates are larger than the forces arising from deformation of the elastic tetrahedra. At larger deformations, the strain energy dominates the interaction energy between the particle and the plates.

9.4 Jammed Packings of Deformable Particles

In previous sections, we described the mechanical properties of individual deformable particles. We will now describe the collective structural and mechanical properties of static, jammed packings of N deformable particles. To generate a jammed packing, we start with a dilute system at packing fraction $\phi = 10^{-3}$, randomly placed particles in a square (cubic) box with side length L in 2D (3D), and periodic boundary conditions in all directions. We isotropically compress the system by decreasing L in small steps $\Delta L/L$ so that the packing fraction increases by $\Delta \phi/\phi < 10^{-3}$. After each compression step, we use the FIRE algorithm⁴⁴ to minimize the total potential energy that includes the shape-energy function and interaction potential energy. We then calculate the pressure P of the energy-minimized packing. If $P < P_t$, we compress the system again, followed by energy minimization. If $P > P_t$, we return to the configuration before the most recent compression step and decrease $\Delta L/L$ by a factor of 2. We continue this process until $1 < P/P_t < 1.01$. We set $\bar{P}_t = 10^{-7}$, where $\bar{P}_t = P_t/(k_a^{2D}a_0)$ in 2D and $P_t/(k_v^{3D}\nu_0)$ in 3D for the dimensionless threshold pressure that signals jamming onset, where a_0 and v_0 are the average rest area and volume in 2D and 3D, respectively. After saving the packing at jamming onset, we compress the packing further to generate overcompressed particle configurations at dimensionless pressures that are logarithmically spaced between 10^{-7} and 10^{-2} .

In this section, we will first describe the calculation of the packing fraction of jammed deformable particle packings in periodic boundary conditions given that deformable particles possess spherical vertices on their surfaces and provide expressions for the components of the stress tensor in systems with periodic boundary conditions given that the shape-energy function of deformable particles includes many-body potentials. We will use these results to show the pressure *versus* packing fraction relation near jamming onset for packings of deformable particles in 2D. We also compare the vibrational density of states of jammed packings of floppy particles, elastic shells, and surface-energy dominated particles with rough interactions in 2D and 3D, by calculating the eigenvalue spectrum of the dynamical matrix.

9.4.1 Calculation of Packing Fraction

The packing fraction ϕ plays a dominant role in controlling the collective mechanical properties of many particulate systems. We will focus on systems near jamming onset, where overlaps between deformable particles are small compared to the particle size. In this case, the packing fraction is the total area (volume) occupied by the particles divided by the area (volume) of the confining boundaries. The area (volume) of each particle is determined by the edges of the particle that define the interaction potential between particles in eqn (9.3) for rough particles and eqn (9.5) for smooth particles. In this subsection, we describe the calculation of the packing fraction ϕ for collections of N rough deformable particles in a square box with side length L in 2D with periodic boundary conditions and validate the method using Monte-Carlo integration. Calculations of ϕ for deformable particles with smooth interactions and in 3D can be obtained using similar methods.

The area occupied by a collection of 2D deformable particles with rough interactions is the sum of the areas of the polygons and vertices for each particle (see Figure 9.12(a)). However, we must subtract off the areas of regions that are double-counted for overlaps that occur between two vertices on a given particle, overlaps between the vertices and polygon on a given particle, as well as overlaps between vertices on different particles. If the vertices on a given deformable particle do not overlap significantly, $0.1 < r_{\mu i,\mu j}/\sigma_{\mu} < 1$, we only need to consider overlaps between pairs of vertices and a single vertex overlap with each polygon. The area of a collection of deformable particles is

$$A_{\text{particles}} = A_{\text{polygon}} + A_{\text{vertices}} - A_{\text{sector}} - A_{\text{pair}}, \tag{9.18}$$

where $A_{\text{polygon}} = \sum_{\mu=1}^{N} a_{\mu}$, is the area of the polygon for each particle (see Figure 9.12(b)). The total area of the vertices for all particles is

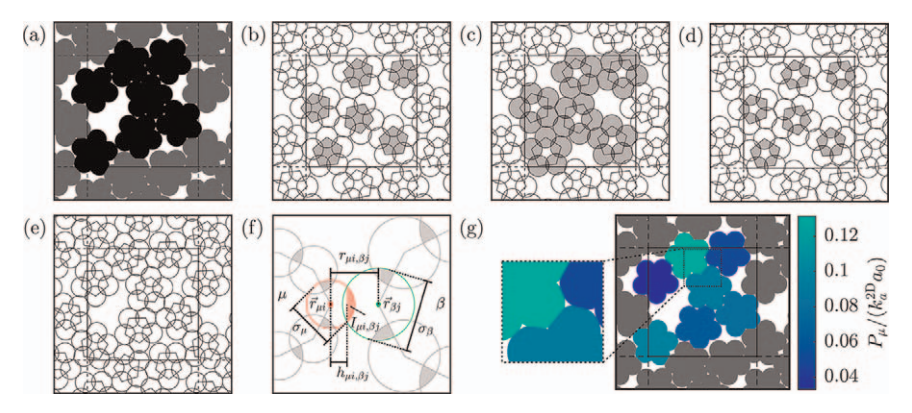


Figure 9.12 (a) A jammed packing of N=7 rough, deformable particles. We show the area of the particles $A_{\text{particles}}$ in the main simulation cell (black), unoccupied area (white), and area of particles in the image cells (gray). The packing fraction ϕ is the ratio of the area in black to the total area of the main cell. The area of the particles has four contributions: $A_{\text{particles}} = A_{\text{polygon}} + A_{\text{vertices}} - A_{\text{sector}} - A_{\text{pair}}$. (b) A_{polygon} is shaded gray. (c) The area of the vertices in the main cell A_{vertices} is shaded gray. (d) The regions A_{sector} that are counted both in the polygon and vertex areas are shaded gray. (e) The vertex-vertex overlaps outside of the particle polygons A_{pair} are shaded gray. (f) A close-up of vertex i (red) on particle μ overlapping with vertex j (green) on particle β . σ_{μ} and σ_{β} are the diameters of the vertices, $r_{\mu i,\beta j}$ is their separation, and $h_{\mu i,\beta j}$ is the distance from $\vec{r}_{\mu i}$ to the planar interface with vertex j on particle β . $I_{\mu i,\beta j}$ is the red-shaded area. Intraparticle vertex-vertex overlaps outside of the particle polygons are shown in gray; these regions correspond to the first term in eqn (9.19). (g) Each particle area A_{μ} is shaded according to the local pressure $P_{\mu} = \text{Tr}(\bar{\Sigma}_{\mu})/2$ (in units of $k_a^{\text{2D}}a_0$, where a_0 is the average preferred area). The close-up shows the planar interfaces between several vertices on different particles. In (a)-(e), and (g), the main cell is indicated by a solid black line, and the image cells are indicated by dashed black lines.

$$A_{\text{vertices}} = \sum_{\mu=1}^{N} \sum_{i=1}^{N_{\mu}} \pi \sigma_{\mu}^2 / 4$$
 (see Figure 9.12(c)). $A_{\text{sector}} = \sum_{\mu=1}^{N} \sum_{i=1}^{N_{\mu}} \sigma_{\mu}^2 (\pi - \theta_{\mu i}) / 8$ is

the area of the overlaps between each vertex and the polygon of the particle to which they belong, as shown in Figure 9.12(d). The area of the overlaps between the vertices that occur outside of the particle polygons is

$$A_{\text{pair}} = \sum_{\mu=1}^{N} \sum_{i=1}^{N_{\mu}} I_{\mu i, \mu(i+1)} + \sum_{\mu=1}^{N} \sum_{i=1}^{N_{\mu}} \sum_{\substack{\beta=1\\\beta \neq \mu}}^{N_{\mu}} \sum_{j=1}^{N_{\beta}} I_{\mu i, \beta j}, \tag{9.19}$$

which includes both intra- and interparticle vertex-vertex overlaps and is shaded gray in Figure 9.12(e). In eqn (9.19), $I_{\mu i,\beta j}$ is the area of one of the two circular segments (with radius $\sigma_{\mu}/2$) defined by the points where overlapping

vertices i on particle μ and j on particle β intersect.⁴⁵ The area of overlap between vertex i on particle μ and vertex j on particle β is

$$I_{\mu i, \beta j} = \Theta(\sigma_{\mu \beta} - r_{\mu i, \beta j}) \left[\left(\frac{\sigma_{\mu}}{2} \right)^{2} \arccos \left(\frac{r_{\mu \beta}^{2} - \left(\frac{\sigma_{\beta}}{2} \right)^{2} + \left(\frac{\sigma_{\mu}}{2} \right)^{2}}{\sigma_{\mu} r_{\mu \beta}} \right) - \frac{r_{\mu \beta}^{2} - \left(\frac{\sigma_{\beta}}{2} \right)^{2} + \left(\frac{\sigma_{\mu}}{2} \right)^{2}}{2r_{\mu \beta}} \sqrt{\left(\frac{\sigma_{\mu}}{2} \right)^{2} - \left(\frac{r_{\mu \beta}^{2} - \left(\frac{\sigma_{\beta}}{2} \right)^{2} + \left(\frac{\sigma_{\mu}}{2} \right)^{2}}{2r_{\mu \beta}} \right)^{2}} \right].$$

$$(9.20)$$

The first term in the square brackets is the area of the circular sector defined by vertex i and the intersection points with vertex j, and the second term removes the area of the triangle defined by the intersection points and $\vec{r}_{\mu i}$. The Heaviside function ensures that $I_{\mu i,\beta j}$ only contributes to A_{pair} when vertex i and j overlap. (See the red-shaded region in Figure 9.12(f).) In eqn (9.19), the first term is a sum over adjacent vertices in each particle, and since all vertices on particle μ have the same diameter, $I_{\mu i,\mu}(i+1)$ is half the overlap between vertex i and vertex i+1. We only use this half overlap when calculating A_{pair} because only half of the intersection occurs outside the polygon of particle μ . In the second term in eqn (9.19), the double sum

 $\sum\limits_{eta=1,eta
eq\mu}^{N}\sum\limits_{j=1}^{N_{eta}}I_{\mu i,eta j}$ is the size of the double-counted region we associate with

vertex i on particle μ from overlaps with vertices on other particles. Thus, the area attributed to a single deformable particle μ is

$$A_{\mu} = a_{\mu} + \sum_{i=1}^{N_{\mu}} \frac{\pi}{4} \sigma_{\mu}^{2} - \sum_{i=1}^{N_{\mu}} \sigma_{\mu}^{2} \frac{(\pi - \theta_{\mu i})}{8} - \sum_{i=1}^{N_{\mu}} I_{\mu i, \mu(i+1)} - \sum_{i=1}^{N_{\mu}} \sum_{\substack{\beta = 1 \\ \beta \neq \mu}}^{N} \sum_{j=1}^{N_{\beta}} I_{\mu i, \beta j}.$$

$$(9.21)$$

While it is possible to make other choices concerning the attribution of double-counted area between vertices on different particles, this choice reflects the idea that the particles deform such that two contacting vertices form a planar interface, and as a result the area occupied by vertex i should be reduced by $I_{\mu i,\beta j}$. In Figure 9.12(g), the blue- and green-shaded regions indicate A_{μ} (eqn (9.21)) for each particle.

Using eqn (9.18), the packing fraction is defined as

$$\phi = A_{\text{particles}}/L^2. \tag{9.22}$$

In Table 9.2, we compare the analytic expressions for ϕ and the four contributions to $A_{\rm particles}$ (*i.e.* $A_{\rm polygon}$, $A_{\rm vertices}$, $A_{\rm sector}$, and $A_{\rm pair}$) to those found using Monte-Carlo integration for the deformable particle packing in

Table 9.2 The packing fraction $\phi = A_{\rm particles}/L^2$ and the four contributions to $A_{\rm particles} = A_{\rm polygon} + A_{\rm vertices} - A_{\rm sector} - A_{\rm pair}$ (eqn (9.18)) for the deformable particle packing in Figure 9.12. For ϕ and each area contribution, we compare the analytical expressions in the middle row to those obtained from Monte-Carlo integration in the bottom row. The errors in the Monte-Carlo integration scale as $\sim N_{\rm m}^{-1/2}$, where $N_{\rm m}$ is the number of Monte-Carlo trials.

Method	$\phi = A_{\text{particles}}/L^2$	$A_{ m polygon}/L^2$	$A_{ m vertex}/L^2$	$A_{ m sector}/L^2$	$A_{ m pair}/L^2$
Analytic Monte- Carlo	$0.8397 \\ 0.8391 \pm 0.0008$	$0.276 \\ 0.276 \pm 0.001$	$\begin{array}{c} 0.8648 \\ 0.8642 \pm 0.0008 \end{array}$	$0.259 \\ 0.260 \pm 0.001$	$0.0415 \\ 0.0410 \pm 0.0004$

Figure 9.12(a). For example, we find $\phi=0.8397$ using eqn (9.22) and $\phi=0.8391\pm0.0008$ using Monte-Carlo integration for this deformable particle packing. The packing in Figure 9.12(a) contains elastic shell particles with $k_1^{\rm 2D}/k_{\rm c}=2$, $k_{\rm b}^{\rm 2D}/(k_{\rm c}\sigma^2)=0.3$, and $k_{\rm a}^{\rm 2D}a_0^2/(k_{\rm c}\sigma^2)=0.9$ with rough interactions, $N_{\rm u}=5$, N=7, and $A_0^{\rm 2D}=A_{\rm min}^{\rm 2D}$.

9.4.2 Stress Tensor for Deformable Particles in Periodic Boundary Conditions

The stress tensor $\bar{\Sigma}$ of a jammed packing of deformable particles describes the mechanical response of the packing. The stress tensor is symmetric with d(d+1)/2 independent components in d dimensions. The pressure is given by the diagonal elements of the stress tensor, $P = Tr(\bar{\Sigma})/d$, where Tr is the trace. The off-diagonal components of the stress tensor give the shear stress. The stress tensor is straightforward to calculate for systems of point particles with fixed-wall boundary conditions. For periodic boundary conditions, the potential energy (and thus the stress tensor) has an additional dependence on the length of the boundary from the minimum image convention. 46 For systems with *only* pairwise, central potentials, the additional dependence on box length can be captured by summing over each pair interaction and using the main simulation cell position of one particle in the pair and the closest image position of the other particle when calculating each pair interaction's contribution to the stress tensor.⁴⁷ The shape-energy function for deformable particles includes not only pair interactions, but also many-body potentials (see eqn (9.1) and (9.2)). In this section, we will first review expressions for the stress tensor for collections of particles that interact via repulsive pairwise, central potentials with periodic boundary conditions. We then generalize the expressions for the stress tensor for packings of deformable particles to include many-body interactions with periodic boundary conditions. We also discuss a method for defining the stress tensor for each particle that sums to the total stress tensor when averaged over all particles in the system. Using these relations for the stress tensor, we calculate the pressure of deformable particle packings as a function of packing fraction as they are isotropically compressed above jamming onset.

For a 2D system of N elastic disks modeled by point particles with short-range pairwise, central potentials, and fixed-wall boundary conditions, the stress tensor can be defined as

$$\bar{\Sigma}_{ab} = \left\langle \frac{1}{A_{\text{system}}} \sum_{n=1}^{N} \left(m_n \nu_{n,a} \nu_{n,b} + r_{n,a} F_{n,b} \right) \right\rangle, \tag{9.23}$$

where a, b = x, y, $r_{n,a}$ and $v_{n,a}$ are the ath components of the position and velocity vectors for disk n, and m_n is the mass of disk n. $F_{n,b}$ is the bth component of the net force on disk n, A_{system} is the area of the system, and $\langle \cdot \rangle$ gives the ensemble average. In eqn (9.23), the first term is the contribution to the stress tensor from momentum transfer through particle motion, while the second term is the force moment or virial contribution.

However, eqn (9.23) does not hold for systems with periodic boundary conditions.⁴⁷ The stress tensor can be calculated for systems with pairwise interactions in periodic boundary conditions by making a specific choice for the position factor in the force moment. When calculating the contribution to the stress tensor for the pair interaction between disk n and disk m, we use the position of disk n in the main simulation cell, and the closest image position of disk m, since these are the positions used to calculate the interaction potential and forces between disks n and m within the main simulation cell.⁴⁶ Using this method,

$$\bar{\Sigma}_{ab} = \left\langle \frac{1}{A_{\text{system}}} \left(\sum_{n=1}^{N} \left(m_n \nu_{n,a} \nu_{n,b} \right) + \sum_{n=1}^{N-1} \sum_{m=n+1}^{N} \left(r_{n,a}^{n,\text{pair}} F_{nm,b}^{n,\text{pair}} + r_{m,a}^{n,\text{pair}} F_{mn,b}^{n,\text{pair}} \right) \right) \right\rangle,$$
(9.24)

where $r_{n,a}^{n,\mathrm{pair}}$ is ath component of the position vector of disk n in the main simulation cell and $r_{m,a}^{n,\mathrm{pair}}$ is the ath component of the position vector of the closest image of disk m to disk n. $F_{nm,b}^{n,\mathrm{pair}} = -\frac{\partial}{\partial r_{n,b}^{n,\mathrm{pair}}} U_{nm}^{\mathrm{pair}}$ is the bth com-

ponent of the force on disk n from the pair force on disk n from disk m and $F_{mn,b}^{n,\mathrm{pair}} = -\frac{\partial}{\partial r_{mh}^{n,\mathrm{pair}}} U_{nm}^{\mathrm{pair}}$ is the bth component of the pair force on disk m from

disk n. U_{nm}^{pair} is the pair potential between disks n and m using the minimum image distance between them. Eqn (9.24) can then be rearranged as

$$\bar{\Sigma}_{ab} = \left\langle \frac{1}{A_{\text{system}}} \left(\sum_{n=1}^{N} m_n \nu_{n,a} \nu_{n,b} - \sum_{n=1}^{N-1} \sum_{m=n+1}^{N} r_{nm,a}^{n,\text{pair}} F_{nm,b}^{\text{pair}} \right) \right\rangle, \tag{9.25}$$

where $r_{nm,a}^{n,\mathrm{pair}} = r_{m,a}^{n,\mathrm{pair}} - r_{n,a}^{n,\mathrm{pair}}$, using Newton's third law.

In the case of deformable particles, the total potential energy (and therefore the stress tensor) has two contributions. First, the total potential energy includes pairwise interactions from vertices on different particles, which can be treated using eqn (9.25). The second contribution includes many-body interactions from the shape-energy function $U_{\mu, \rm shape}^{\rm 2D}$. How do the many-body interactions contribute to the stress tensor for systems with periodic boundary conditions? We calculate the stress tensor using the copy of each particle whose center of mass occurs in the main simulation cell. We use the positions of these copies when calculating the shape-energy contribution to the force moment. This choice ensures, as required, that the contributions from the shape-energy function for each particle appear only once in the stress tensor and that the positions used to calculate the force moment correspond to those used to calculate the shape-energy functions. ⁴⁶ The stress tensor of a system of N 2D rough deformable particles is

$$\bar{\Sigma}_{ab} = \left\langle \frac{1}{A_{\text{system}}} \left(\sum_{\mu=1}^{N} \sum_{i=1}^{N_{\mu}} \left(m_{\mu i} v_{\mu i,a} v_{\mu i,b} + \tilde{r}_{\mu i,a} F_{\mu i,b}^{\text{shape}} \right) \right. \right.$$

$$-\sum_{\mu=1}^{N-1} \sum_{i=1}^{N_{\mu}} \sum_{\beta=\mu+1}^{N} \sum_{j=1}^{N_{\beta}} r_{\mu i, \beta j, a} F_{\mu i, \beta j, b}^{\text{rough}} \right) , \tag{9.26}$$

where $m_{\mu i}$ is the mass of vertex i on particle μ and $v_{\mu i,a}$ is the ath component of the velocity vector of vertex i on particle μ . $\tilde{r}_{\mu i,a}$ is the ath component of the position vector of vertex i on the copy of particle μ that appears in the main simulation cell. The first term in the double sum is the contribution to the stress tensor from momentum transport via particle motion. The second term is the contribution from the shape-energy function, where $F_{\mu i,b}^{\rm shape} = -\frac{\partial}{\partial \tilde{r}_{\mu i,b}} U_{\mu,\rm shape}^{\rm 2D}$ is the bth component of the net force on vertex i of particle μ arising from shape-energy forces. The quadruple sum is the contribution from each vertex-vertex pair interaction $U_{\mu i,\beta j}^{\rm rough}$, where $r_{\mu i,\beta j,b}$ is the bth component of the separation vector between vertex i on particle μ in the main simulation cell and the closest image of vertex j on particle β and $F_{\mu i,\beta j,b}^{\rm rough} = -\frac{\partial}{\partial r_{\mu i,b}} U_{\mu i,\beta j}^{\rm rough}$ is the bth component of the pair force on vertex i on particle μ from vertex j on β .

A similar formulation for the stress tensor can be developed for smooth interactions between deformable particles in systems with periodic boundary conditions. In this case, the quadruple sum in eqn (9.26) is replaced with three quadruple sums that account for the forces arising from $U_{\mu i, \beta j}^{\rm edge}$, $U_{\mu i, \beta j}^{\rm concave}$, and $U_{\mu i, \beta j}^{\rm convex}$. We use the position of particle β in the main simulation cell given by $\tilde{r}_{\beta j}$ and the closest image of $\vec{r}_{\mu i}$ in eqn (9.6), (9.8), and (9.9).

In static packings of deformable particles in systems with periodic boundary conditions, we can also quantify the stress tensor for each particle μ :

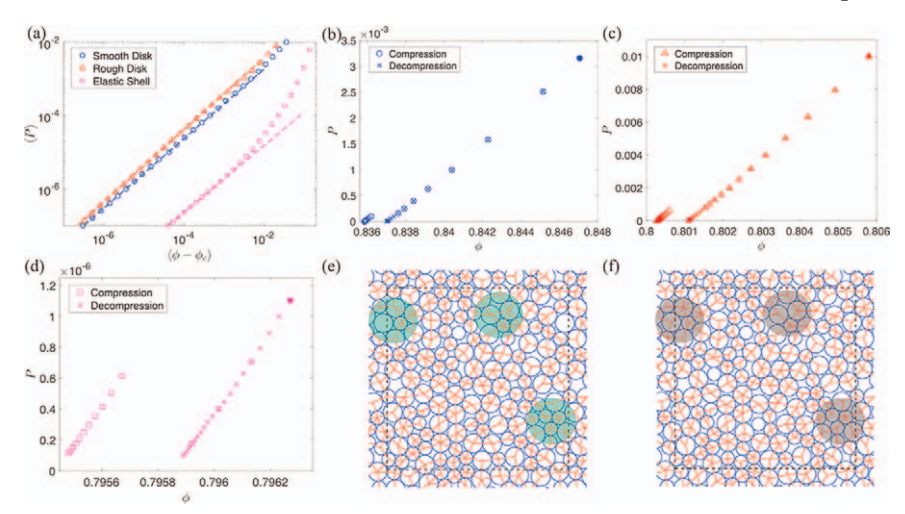
$$\bar{\Sigma}_{\mu,ab} = \left\langle \frac{1}{A_{\mu}} \left(\sum_{i=1}^{N_{\mu}} \tilde{r}_{\mu i,a} F_{\mu i,b}^{\text{shape}} - \sum_{i=1}^{N_{\mu}} \sum_{\substack{\beta=1\\\beta \neq \mu}}^{N} \sum_{j=1}^{N_{\beta}} \frac{h_{\mu i,\beta j}}{r_{\mu i,\beta j}} r_{\mu i,\beta j,a} F_{\mu i,\beta j,b}^{\text{rough}} \right) \right\rangle, \quad (9.27)$$

where A_{μ} is the area of particle μ in eqn (9.21) and $h_{\mu i,\beta j}$ is the distance from vertex i on particle μ to the "contact line" with vertex j on particle β as shown in Figure 9.12(f). The triple sum allocates a fraction of the force moment arising from the interaction between vertex i on particle μ and vertex j on particle β to particle μ that is proportional to $h_{\mu i,\beta j}/r_{\mu i,\beta j}$, which is the fraction of the separation vector $\vec{r}_{\mu i,\beta j}$ that lies within $A_{\mu}^{48,49}$ (see Figure 9.12(f) and (g)).

We emphasize that for this definition of the local stress tensor we assumed that the stresses arising from the shape-energy function occur within the area spanned by the deformable particle. We also chose to distribute the contact stresses along the shortest line between contacting vertices and use the Irving–Kirkwood convention⁵⁰ of assuming that stress from a pair interaction acts along the line between the two points. However, other definitions of local stresses are also valid. In Figure 9.12(g), we show that the local pressure $P_{\mu} = (\bar{\Sigma}_{\mu})/2$ on each particle varies in static packings of elastic shell particles $(k_1^{\text{2D}}/k_c=2,\ k_b^{\text{2D}}/k_c=0.3,\ \text{and}\ k_a^{\text{2D}}/k_c=0.9)$ with rough interactions, $N_{\mu}=5$, N=7, and $\mathcal{A}_0^{\text{2D}}=\mathcal{A}_{\min}^{\text{2D}}$. The total stress tensor of the system can be obtained by calculating the area-weighted sum of the single particle

stress tensors over all particles:
$$\bar{\Sigma} = \sum_{\mu=1}^{N} A_{\mu} \bar{\Sigma}_{\mu} / A_{\text{system}}$$
.

Obtaining the pressure P and packing fraction ϕ of static packings of deformable particles is crucial to understanding their mechanical properties. For instance, in mechanically stable, amorphous packings of soft, bidisperse disks in 2D that interact via purely repulsive linear spring potentials with periodic boundary conditions, the pressure $\langle P \rangle$ (averaged over an ensemble of packings) increases with excess packing fraction $\phi - \phi_c$ above jamming onset: $\langle P \rangle = B \langle (\phi - \phi_c) \rangle^{\zeta}$, where ϕ_c is the packing fraction at jamming onset, B is the bulk modulus, and $\zeta = 1^{52}$ (see Figure 9.13(a)). In the case of static packings of bidisperse elastic shell particles with $\mathcal{A}_{0}^{\mathrm{2D}} = \mathcal{A}_{\min}^{\mathrm{2D}}, \ k_{\mathrm{a}}^{\mathrm{2D}} > 0, \ k_{\mathrm{l}}^{\mathrm{2D}} > 0, \ k_{\mathrm{b}}^{\mathrm{2D}} > 0, \ \text{and} \ \gamma^{\mathrm{2D}} = 0, \ \text{we also find} \ \langle P \rangle = B \langle \phi - \phi_{\mathrm{c}} \rangle$ at small pressures as shown in Figure 9.13(a). However, at large pressures, the deformability of the elastic shell particles plays an important role and $\langle P \rangle$ increases nonlinearly with $\langle \phi - \phi_c \rangle$. To determine whether the nonlinearity is caused by the surface roughness of the particles, we also performed isotropic compression of static packings of rough disks that do not change shape with the same number of vertices $N_{\mu} = 20$ as the elastic shells. Each rough disk is modeled as a regular polygon with the associated vertices that move together as a rigid body, such that the total potential energy of the packing obeys



(a) Ensemble-averaged pressure $\langle P \rangle$ (in units of $k_{\rm a}^{\rm 2D} a_0$) versus the Figure 9.13 deviation in packing fraction $\langle \phi - \phi_c \rangle$ from jamming onset at ϕ_c during compression for N = 128 (a) smooth disks with purely repulsive linear spring interactions (blue circles), rough disks (red triangles), and elastic shell particles with $A_0^{\text{2D}} = A_{\text{min}}^{\text{2D}}$, $k_a^{\text{2D}} > 0$, $k_b^{\text{2D}} > 0$, $k_b^{\text{2D}} > 0$, and $\gamma^{2D} = 0$ (magenta squares). The smooth disk packing is bidisperse with half large disks, half small disks, and diameter ratio of 1.4. The rough disk and elastic shell particle packings are also bidisperse with half large, half small, and polygon diameter ratio of 1.4. The results are averaged over 500 packings. The dashed lines show linear fits to $\langle P \rangle = B \langle \phi - \phi_c \rangle$, where B = 0.14, 0.36, and 10^{-3} ($\phi_c = 0.836$, 0.79, and 0.783) for smooth disks, rough disks, and elastic shells, respectively. P versus ϕ for individual static packings for the same systems in (a): (b) smooth disks (circles and crosses), (c) rough disks (triangles and crosses), and (d) elastic shells (squares and crosses). The circles, triangles, and squares show results for static packings compressed starting from jamming onset. The crosses show results for packings decompressed from packings that were originally compressed to the ϕ indicated by the filled symbols. Static packings of smooth disks (e) before and (f) after a rearrangement that causes a change in the contact network (indicated by red lines) following compression by $\Delta\phi \approx 10^{-5}$. The three green (before) and gray (after) regions highlight particle rearrangements.

eqn (9.3).⁴¹ For both packings of smooth and rough disks, we find linear behavior, $\langle P \rangle = B \langle \phi - \phi_c \rangle$, for the ensemble-averaged pressure *versus* packing fraction relation. For individual static packings, irreversible particle rearrangements occur during compression, which cause discontinuities in the pressure *versus* packing fraction relation as shown in Figure 9.13(b)-(d). Note that static packings before and after particle rearrangements possess different ϕ_c . The ensemble-averaged $\langle P \rangle$ *versus* $\langle \phi - \phi_c \rangle$ averages over the rearrangement events giving a smoothed representation of the pressure *versus* packing fraction relation. See an

example of compression-induced particle rearrangements in static packings of smooth disks in Figure 9.13(e) and (f).

9.4.3 Vibrational Density of States

The vibrational response of individual deformable particles, as well as mechanically stable packings of deformable particles, can be obtained by calculating the eigenmodes of the dynamical matrix M, which gives the second derivatives of the total potential energy U with respect to the vertex positions:

$$M_{\mu i,\beta j} = \frac{\partial^2 U}{\partial \vec{r}_{\mu i} \partial \vec{r}_{\beta j}}.$$
 (9.28)

For a system with $N_{\rm dof}$ degrees of freedom, M is a $N_{\rm dof} \times N_{\rm dof}$ matrix with $N_{\rm dof}$ eigenvalues λ_k and eigenvectors \hat{e}_k , where k ranges from 1 to $N_{\rm dof}$ and $\hat{e}_k \cdot \hat{e}_k = 1$. We will report dimensionless eigenvalues $\tilde{\lambda}_k = \lambda_k/\left(k_{\rm a}^{\rm 2D}a_0\right)$ in 2D and $\tilde{\lambda}_k = \lambda_k/\left(k_{\rm v}^{\rm 3D}(\nu_0)^{4/3}\right)$ in 3D, where a_0 and ν_0 are the average equilibrium area and volume of the deformable particles in 2D and 3D, respectively. The vibrational response can be used to determine the necessary conditions for rigidity of a single particle, as well as the collective rigidity of particle packings. For example, packings of spherical particles become mechanically stable with no non-trivial zero eigenmodes when they are isostatic, 53,54 and the number of interparticle contacts (that give rise to $N_{\rm c}$ constraints) matches the number of degrees of freedom $N_{\rm dof}$.

A deformable particle in 2D with N_{μ} vertices has $N_{\rm dof} = 2N_{\mu}$ degrees of freedom. The shape-energy function for floppy particles with $\mathcal{A}_0^{\rm 2D} > \mathcal{A}_{\rm min}^{\rm 2D}$, $k_a^{\rm 2D} > 0$, $k_b^{\rm 2D} = 0$, and $\gamma^{\rm 2D} = 0$ imposes $N_{\rm c} = N_{\mu} + 1$ constraints. Hence, floppy particles have $N_{\rm dof} - N_{\rm c} = N_{\mu} - 1$ unconstrained degrees of freedom, which matches the number of zero eigenmodes of M as shown in Figure 9.14(a). (Note that three of the $N_{\mu} - 1$ zero modes correspond to two rigid translational modes and one rotational mode.) To remove the non-trivial zero energy modes in a single deformable particle, we can either increase the number of constraints without prestress or induce prestress in the particle, e.g. by setting $k_{\rm b}^{\rm 2D} > 0$ with $\theta_{\mu i0} = 2\pi/N_{\mu}$ for all i (elastic shell) or setting $k_{\rm b}^{\rm 2D} = 0$ and $\gamma^{\rm 2D} > 0$ (surface-energy dominated particle). Note that both elastic shells and surface-energy dominated particles are circular when they are not subjected to external stresses. Indeed, M for an elastic shell and for a surface-energy dominated particle possesses only three trivial zero modes as shown in Figure 9.14(a).

In Figure 9.14(b), we show the eigenvalue spectrum $\tilde{\lambda}_k$ of M for static packings of "floppy" particles, elastic shells, and surface-energy dominated particles with rough interactions at jamming onset in 2D. In addition to the two zero modes that correspond to rigid translations arising from periodic boundary conditions, we find that low-frequency modes occur in "floppy" particle packings that are absent in packings of elastic shells and surface-energy dominated particles. These low-frequency modes in floppy-particle packings have been identified as

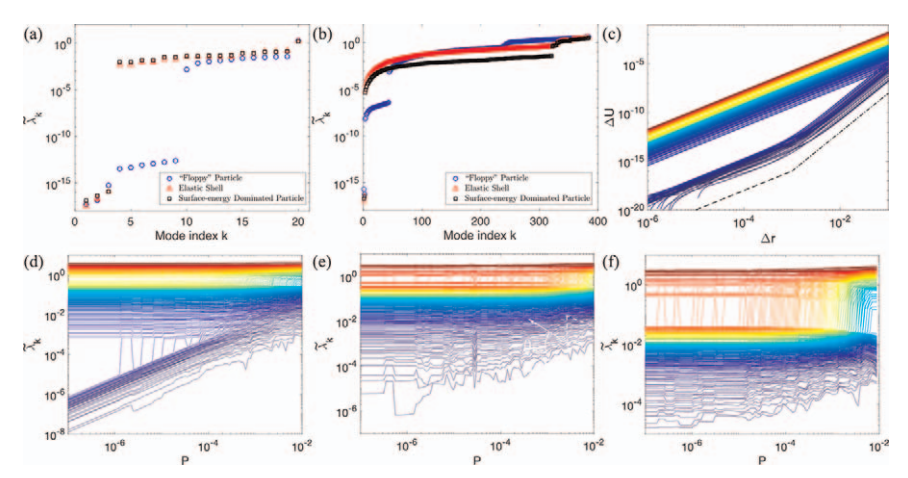


Figure 9.14 (a) Eigenvalues λ_k of the dynamical matrix M for a "floppy" particle (blue circles), elastic shell (red triangles), and surface-energy dominated particle (black squares) with $N_{\mu} = 10$ vertices in 2D. The "floppy" particle has $\mathcal{A}_{0}^{2D} = 1.04$, $k_{a}^{2D} > 0$, $k_{1}^{2D} > 0$, $k_{b}^{2D} = 0$, and $\gamma^{2D} = 0$. The elastic shell has $\mathcal{A}_{0}^{2D} = \mathcal{A}_{\min}^{2D}$, $k_{a}^{2D} > 0$, $k_{1}^{2D} > 0$, $k_{b}^{2D} > 0$, and $\gamma^{2D} = 0$. The surface-energy dominated particle has $\mathcal{A}_{0}^{2D} = \mathcal{A}_{\min}^{2D}$, $\mathcal{A}_{a}^{2D} > 0$, and $\mathcal{A}_{b}^{2D} = 0$. $k_{\rm l}^{\rm 2D} > 0$, $k_{\rm b}^{\rm 2D} = 0$, and $\gamma^{\rm 2D} > 0$. The eigenvalues $\tilde{\lambda}_{\rm k}$ are sorted in ascending order. Modes with $\tilde{\lambda}_k < 10^{-13}$ are considered "zero" modes. (b) $\tilde{\lambda}_k$ for jammed packings of "floppy" (blue circles), elastic shell (red triangles), and surface-energy dominated (black squares) particles in 2D at pressure $P = 10^{-7}$ in units of $k_a^{2D} a_0$, where a_0 is the equilibrium area. Each packing has N = 16 particles, half with $N_{\mu}^{\text{small}} = 10$ and half with $N_{\mu}^{\text{large}} = 14$ vertices. (c) Change in potential energy ΔU (in units of $k_a^{2D} a_0^2$ in the packing of "floppy" particles in (b) when it is perturbed by amplitude Δr in units of $(a_0)^{1/2}$ along each eigenmode of M. The dot-dashed (dashed) line represents $\Delta U \sim (\Delta r)^{\kappa}$ with $\kappa = 4$ (2). $\tilde{\lambda}_k$ plotted versus pressure P for the packings in (b) containing (d) "floppy" particles, (e) elastic shells, and (f) surface-energy dominated particles. The colors in (c)–(f) indicate the mode indexes from k=1(dark blue) to $N(N_{\mu}^{\text{small}} + N_{\mu}^{\text{large}}) = 384$ (dark red).

"quartic" modes. When perturbing a floppy-particle packing along a quartic mode with amplitude Δr , the change in potential energy ΔU first scales quadratically with Δr at small Δr and then quartically at large Δr (see Figure 9.14(c)). In comparison, $\Delta U \propto (\Delta r)^2$ for all Δr for higher frequency quadratic modes. (Note that quartic modes have also been observed in jammed packings of non-spherical particles^{55,56} and "breathing" particles with size degrees of freedom.⁵⁷) The number of quartic modes equals the number of missing contacts $N_{\rm m} = 2NN_{\mu} - 1 - N_{\rm vv}$, where $N_{\rm vv}$ is the number of vertex-vertex contacts between deformable particles in the packing. Further, since quartic modes arise from a higher-order expansion of the potential energy with respect to the vertex positions, they are pressure-dependent. In Figure 9.14(d),

we show that $\tilde{\lambda}_k$ increase linearly with pressure for quartic modes, while $\tilde{\lambda}_k$ are constant with pressure for quadratic modes. Since packings of elastic shells and surface-energy dominated particles do not possess quartic modes, their $\tilde{\lambda}_k$ do not increase strongly with pressure, as shown in Figure 9.14(e) and (f).

We have also studied the vibrational response in 3D for a single (1) "floppy" particle, $\mathcal{A}_0^{\text{3D}} > \mathcal{A}_{\min}^{\text{3D}}$, $k_v^{\text{3D}} > 0$, $k_a^{\text{3D}} > 0$, $k_b^{\text{3D}} = 0$, and $\gamma^{\text{3D}} = 0$; (2) elastic shell, $\mathcal{A}_0^{\text{3D}} = \mathcal{A}_{\min}^{\text{3D}}$, $k_v^{\text{3D}} > 0$, $k_a^{\text{3D}} > 0$, with $\theta_{\mu e0}$ that correspond to the equilibrium bending angles for a polyhedron with $\mathcal{A}_0^{\text{3D}} = \mathcal{A}_{\min}^{\text{3D}}$, and $\gamma^{\text{3D}} = 0$; and (3) surface-energy dominated particle, $\mathcal{A}_0^{\text{3D}} = \mathcal{A}_{\min}^{\text{3D}}$, $k_v^{\text{3D}} > 0$, $k_a^{\text{3D}} > 0$, $k_b^{\text{3D}} = 0$, and $\gamma^{\text{3D}} > 0$. In Figure 9.15(a), we show that only the "floppy" particle (with $N_\mu = 42$ vertices) possesses non-trivial zero modes $(N_{\text{dof}} - N_{\mu f} - 1 = 3N_\mu - (2N_\mu - 4) - 1 = N_\mu + 3 = 45)$. The elastic shell and surface-energy dominated particles possess only six zero modes, which correspond to three rigid translations and rotations. Only packings of floppy particles exhibit quartic modes as shown in Figure 9.15(b), where ΔU increases as $(\Delta r)^4$ along a quartic eigenmode²⁸ (Figure 9.15(c)). Quadratic and quartic modes in 3D packings of deformable particles show the same pressure dependence as those in 2D (see Figure 9.15(d)–(f)).

In previous studies, we have shown that the presence of quartic vibrational modes strongly influences the pressure dependence of the shear modulus G of jammed packings. To measure G for packings of deformable particles, we apply a series of small simple shear strains $\Delta\gamma$, with each simple shear strain followed by potential energy minimization, and calculate the resulting shear stress. For each simple shear strain step, we apply the following transformation to the vertex positions consistent with Lees-Edwards boundary conditions: $x'_{\mu i} = x_{\mu i} + \Delta\gamma y_{\mu i}$ with $\Delta\gamma = 5 \times 10^{-9}$. Following the shear strain step and energy minimization, we calculate the shear stress $\bar{\Sigma} = -\bar{\Sigma}_{xy}$ and shear modulus $G = \partial \bar{\Sigma}/\partial\gamma$.

For jammed packings of purely repulsive smooth disks and spheres, the ensemble-averaged shear modulus $\langle G \rangle$ obeys the following scaling relation with pressure P:

$$\frac{\langle G \rangle - G_0}{G_0} = \frac{\left(\frac{P}{P_0}\right)^{\xi}}{1 + c_2 \left(\frac{P}{P_0}\right)^{\xi - \eta}},\tag{9.29}$$

where G_0 , P_0 , and c_2 are constants, and $\xi \approx 1$ and $\eta \approx 0.5$ are scaling exponents. At large P, $\langle G \rangle \sim P^{\eta}$ and the exponent is determined by the scaling of the excess contact number with pressure. For 2D packings of floppy particles in Figure 9.16(a), we find that $\eta \approx 1$ instead of 0.5 due to the presence of quartic modes. $\eta > 0.5$ has been reported previously for jammed packings of non-spherical particles such as ellipses, which also possess quartic modes. We also calculate $\langle G \rangle$ versus P for packings of elastic shells and surface-tension dominated particles, which do not have quartic modes. In these systems, $\eta \approx 0.5$ as shown in Figure 9.16(a). We find similar results

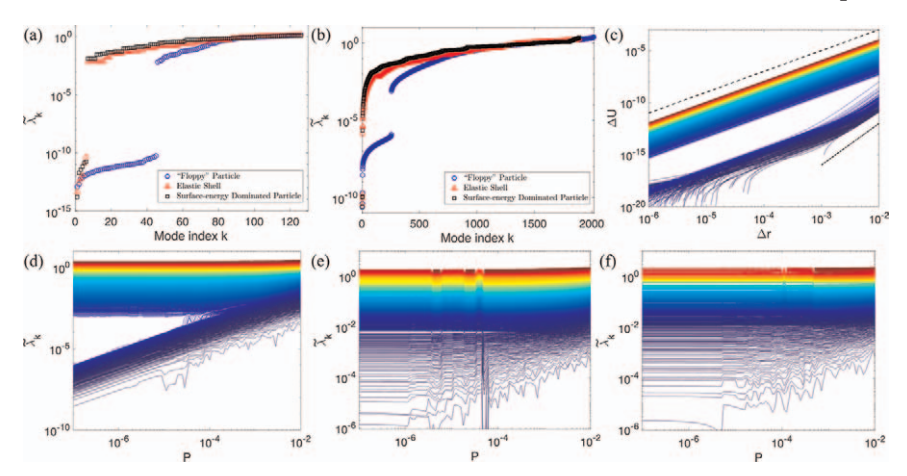


Figure 9.15 (a) Eigenvalues $\tilde{\lambda}_k$ of the dynamical matrix M for a single "floppy" particle (blue circles), elastic shell (red triangles), and surface-energy dominated particle (black squares) with $N_{\mu} = 42$ vertices in 3D. The "floppy" particle has $\mathcal{A}_0^{\mathrm{3D}} = 1.04$, $k_\mathrm{v}^{\mathrm{3D}} > 0$, $k_\mathrm{a}^{\mathrm{3D}} > 0$, and $\gamma^{\mathrm{3D}} = 0$. The elastic shell has $\mathcal{A}_0^{\mathrm{3D}} = \mathcal{A}_{\mathrm{min}}^{\mathrm{3D}}$, $k_\mathrm{v}^{\mathrm{3D}} > 0$, $k_\mathrm{a}^{\mathrm{3D}} > 0$, $k_\mathrm{b}^{\mathrm{3D}} > 0$, θ_med that correspond to the equilibrium bending angles for a polyhedron with $\mathcal{A}_0^{3\mathrm{D}} = \mathcal{A}_{\min}^{3\mathrm{D}}$, and $\gamma^{3\mathrm{D}} = 0$. The surface-energy dominated particle has $\mathcal{A}_0^{3\mathrm{D}} = \mathcal{A}_{\min}^{3\mathrm{D}}$, $k_{\mathrm{v}}^{3\mathrm{D}} > 0$, $k_{\mathrm{a}}^{3\mathrm{D}} > 0$, and $\gamma^{3\mathrm{D}} > 0$. The eigenvalues $\tilde{\lambda}_k$ are sorted in ascending order. Modes with $\tilde{\lambda}_k < 10^{-10}$ are considered "zero" modes. (b) $\tilde{\lambda}_k$ for jammed packings of "floppy" particles (blue circles), elastic shells (red triangles), and surface-energy dominated particles (black squares) in 3D at pressure $P = 10^{-7}$ in units of $k_v^{3D} v_0$, where v_0 is the equilibrium particle volume. Each packing has N=16particles with $N_{\mu} = 42$ vertices. (c) Change in potential energy ΔU (in units of $k_v^{3D} v_0^2$ in the packing of "floppy" particles in (b) when it is perturbed by amplitude Δr in units of $(v_0)^{1/3}$ along each eigenmode of M. The dot-dashed (dashed) line represents $\Delta U \sim (\Delta r)^{\kappa}$ with $\kappa = 4$ (2). $\tilde{\lambda}_k$ plotted *versus* pressure P for the packings in (b) containing (d) "floppy" particles, (e) elastic shells, and (f) surface-energy dominated particles. The colors in (c)–(f) indicate the mode indexes from k=1(dark blue) to $3NN_{\mu} = 2016$ (dark red).

for 3D packings of floppy particles, elastic shells, and surface-energy dominated particles in Figure 9.16(b).

9.5 Summary

In this chapter, we describe the mechanics of single deformable particles and the collective properties of jammed packings of deformable particles using the recently developed deformable particle model. Using the shape-energy function of the deformable particle model we can tune the particle mechanics to consider floppy particles, elastic shells, surface-energy dominated particles, as well as bulk elastic particles. We also introduce rough

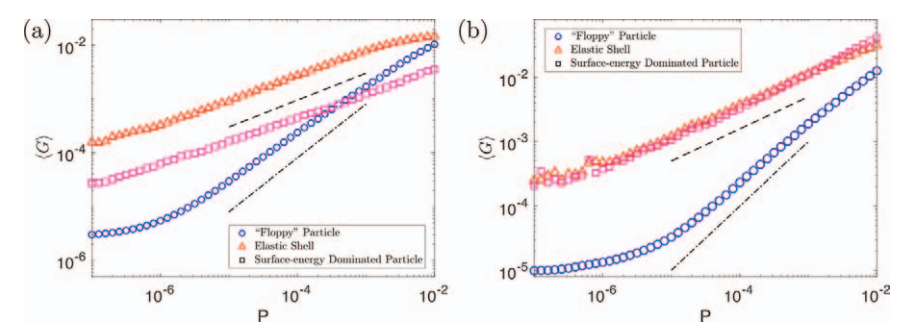


Figure 9.16 Ensemble-averaged shear modulus $\langle G \rangle$ plotted *versus* pressure P for jammed packings of N "floppy" particles (blue circles), elastic shells (red triangles), and surface-energy dominated particles (magenta squares) in (a) 2D and (b) 3D. G and P are expressed in units of $k_{\rm a}^{2D}a_0$ in 2D and $k_{\rm v}^{3D}\nu_0$ in 3D, where a_0 and ν_0 are the equilibrium particle area and volume in 2D and 3D, respectively. The dashed and dash-dotted lines in (a) and (b) have slopes of 0.5 and 1, respectively. N=256 in 2D and 128 in 3D and $\langle G \rangle$ is averaged over 500 packings.

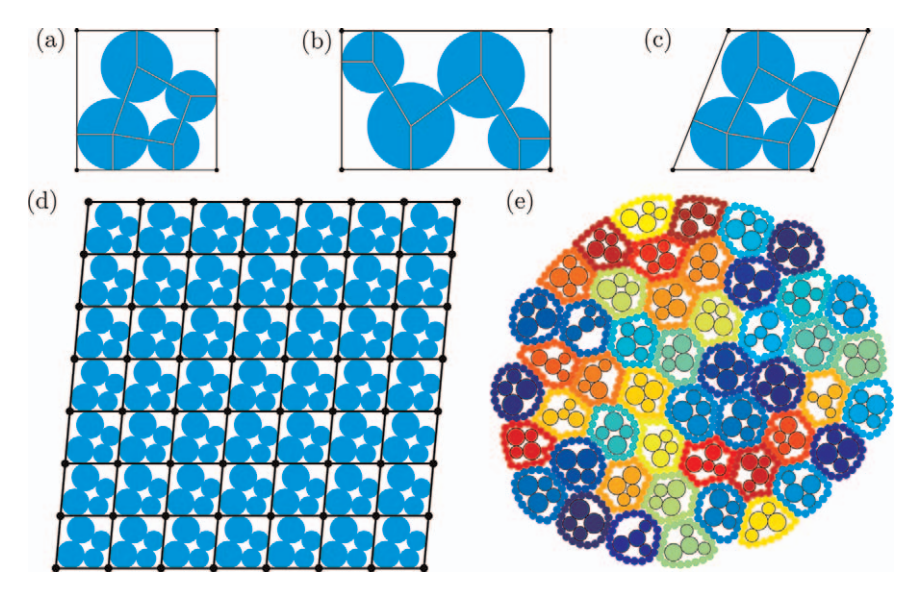


Figure 9.17 Jammed bidisperse disk packings with N=4 in fixed (a) square, (b) rectangular, and (c) parallelogram-shaped boundary conditions. (d) Illustration of a tessellation containing $N_t=49$ cells of the same jammed bidisperse disk packing in (c) with N=4 and fixed parallelogram-shaped boundary conditions. (e) Illustration of a tessellation containing $N_t=49$ cells of jammed bidisperse disk packings within deformable boundaries. The different colors indicate distinct particle-filled cells.

and smooth interaction potential energies in the deformable particle model to control the effective friction coefficient between interacting deformable particles. For the collective properties, we focus on calculations of the packing fraction and stress tensor of packings of deformable particles. We then explore the vibrational properties of jammed packings of deformable particles. We show that jammed packings of floppy particles possess quartic modes, whereas packings of elastic shells and surface-energy dominated particles do not. The presence of quartic modes in packings of floppy particles gives rise to novel pressure scaling of the shear modulus compared to that for jammed packings of elastic spherical particles.

As discussed in the introduction, the deformable particle model can be used to simulate a wide range of physical, biological, and human-engineered systems. Here, we highlight a future application of the deformable particle model to describe the mechanics of soft robotic systems. In most studies of soft particulate materials, the boundaries have a fixed shape, such as squares or rectangles in 2D, as shown in Figure 9.17 (a)–(c). In previous studies, ⁶⁰ we showed that particle packings in fixed boundaries can be used as cells to form a large tessellation (see Figure 9.17(d)). The shape and mechanics of the boundary will significantly impact the mechanical properties of the tessellation. ⁶¹ In addition, particle-filled cells with deformable boundaries can be used to form curved or flexible tessellations as shown in Figure 9.17(e). To begin to address the question of what types of particle packings can occur within deformable boundaries, we show preliminary

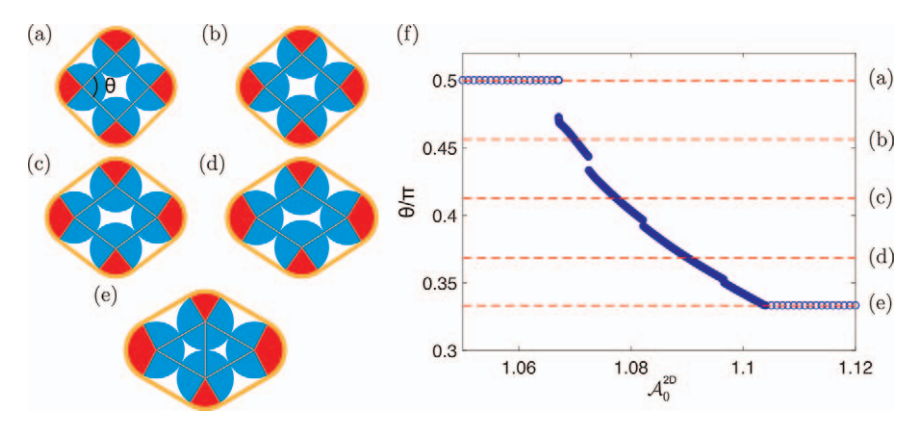


Figure 9.18 (a)–(e) All jammed packings of N=4 monodisperse disks (blue disks) inside a deformable boundary (yellow band) with $N_{\mu}=100$ vertices, $k_{\rm l}^{\rm 2D}>0,~k_{\rm a}^{\rm 2D}=0,~k_{\rm b}^{\rm 2D}=0,~{\rm and}~\gamma^{\rm 2D}=0.$ Red lines (areas) indicate contacts between disks (disks and the boundary). θ gives the smaller of the interior angles of the parallelogram formed by the contacting disks. (f) θ for jammed N=4 monodisperse disk packings with a deformable boundary with $N_{\mu}=100$ vertices, $k_{\rm l}^{\rm 2D}>0,~k_{\rm a}^{\rm 2D}>0,~k_{\rm b}^{\rm 2D}=0,$ and $\gamma^{\rm 2D}=0$ plotted as a function of the preferred shape parameter $\mathcal{A}_0^{\rm 2D}$ of the deformable boundary. The red dashed lines correspond to θ for the packings shown in (a)–(e).

results for jammed monodisperse disk packings within a floppy deformable boundary with $k_1^{\rm 2D} > 0$, $k_a^{\rm 2D} = 0$, $k_b^{\rm 2D} = 0$, and $k_b^{\rm 2D} = 0$. In this case, we find only five possible jammed packings (Figure 9.18(a)–(e)). After including an area constraint on the deformable boundary, *i.e.* $k_a^{\rm 2D} > 0$, which models filling the interior with fluid, we find a nearly continuous range of jammed packings as a function of the preferred shape parameter $\mathcal{A}_0^{\rm 2D}$ of the boundary (see Figure 9.18(f)). One can imagine developing a method to actuate from one of the packings to another in the continuous range for locomotion and gripping applications in soft robotics. The discontinuities in the shape of the disk packing as a function of $\mathcal{A}_0^{\rm 2D}$ in Figure 9.18(f) can arise from a combination of the finite number of vertices included in the boundary and the use of frictionless disks.

9.6 Appendix A

9.6.1 Maximum Effective Friction Coefficient for the Smooth Interaction Potential

In this appendix we calculate the maximum friction coefficient for two elastic shells with smooth interactions undergoing a simple shear test. In Figure 9.8(d), we show $\mu_{\rm eff}(x_{\beta\mu})$ for this system. We find that the maximum effective friction coefficient $\mu_{\rm eff}^{\rm m}$ occurs in the configuration indicated by the star in Figure 9.8(d), between frames 4 and 5 in Figure 9.8(c).

The regime for the maximum friction coefficient between smooth particles in the simple shear test occurs when (1) the right vertex on the top edge of particle β interacts with the bottom vertex on particle μ and (2) the lowest vertex on particle μ is in contact with the top edge of particle β (see Figure 9.19(a) and (b)). In this configuration, the net force from particle β on particle μ is

$$\vec{F}_{\mu\beta} = \vec{F}_{\mu\beta}^{\text{convex}} + \vec{F}_{\mu\beta}^{\text{edge}}, \qquad (9.30)$$

where $\vec{F}_{\mu\beta}^{\, {
m convex}} = \vec{\nabla}_{\vec{r}_{\mu t}} U_{\mu t, \beta r}^{\, {
m convex}}/2$ is the contribution from the vertex-vertex interaction between the vertex r, the top right vertex on particle β , and vertex t, the bottom vertex on particle μ (Figure 9.19(c)), and $\vec{F}_{\mu\beta}^{\, {
m edge}} = \vec{\nabla}_{\vec{r}_{\mu t}} U_{\mu t, \beta (r+1)}^{\, {
m edge}}/2$ is the contribution from the interaction between vertex t on particle μ and edge t+1 on particle t0 (Figure 9.19(d)).

To investigate the dependence of the friction coefficient on the interparticle overlap and horizontal displacement in this regime, we calculated $\mu_{\rm eff}$ while varying $\vec{r}_{\beta r,\mu t} = \vec{r}_{\mu t} - \vec{r}_{\beta r}$, the displacement between the lower vertex on particle μ and the upper right vertex on particle β , and maintaining fixed particle shape (see Figure 9.19(e)). We varied the x-component of $\vec{r}_{\beta r,\mu t}$ by changing the x-component of $\vec{r}_{\beta r,\mu t}$ by changing the y-component of $\vec{r}_{\beta r,\mu t}$ by changing the y-component of $\vec{r}_{\mu t}$ from configurations that yield the maximum overlap between the two particles to

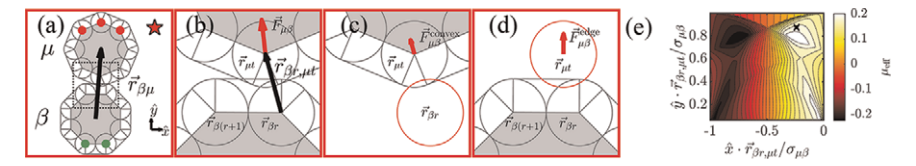


Figure 9.19 (a) Illustration of the configuration of two elastic shells with smooth interactions that corresponds to the star in Figure 9.8(d) with the maximum effective friction coefficient during the simple shear test. The top particle μ and bottom particle β are labeled and $\vec{r}_{\beta\mu}$ gives the separation vector between the centers of the particles. (b) A close-up of the dotted region in (a). The bottom vertex t on particle μ and the upper right vertex r on particle β are labeled, and $\vec{r}_{\beta r,\mu t}$ is the separation vector from vertex r to vertex t. In this configuration, the net force on particle μ from particle β , $\vec{F}_{\mu\beta} = \vec{F}_{\mu\beta}^{\text{convex}} + \vec{F}_{\mu\beta}^{\text{edge}}$, has two contributions. (c) A schematic of the vertex-vertex interaction between vertex r on particle β and vertex t on particle μ , $\vec{F}_{\mu\beta}^{\text{convex}}$. (d) A schematic of the vertex-edge interaction between vertex t on particle μ and edge r+1 on particle β , $\vec{F}_{\mu\beta}^{\text{edge}}$. (e) The effective friction coefficient μ_{eff} as a function of the displacement of particle μ . We vary $\vec{r}_{\beta r,ut}$ by fixing the particle shapes and orientations in (a) and translating particle μ . The horizontal displacements of particle μ range from vertex t occurring directly above vertex r+1 on particle β to above vertex r on particle $\bar{\beta}$, and the vertical displacements range from zero vertical separation between vertex r on particle β and vertex t on particle μ to the zerooverlap limit. The particles remain in contact for all $\vec{r}_{\beta r,\mu t}$ shown. The "x" marks $\vec{r}_{\beta r,\mu t}$ for the starred configuration in (a).

the limit of zero overlap. We find that $\vec{F}_{\mu\beta}$ is nonzero over the full range and the only configurations with $\mu_{\rm eff}=0$ have $\vec{F}_{\mu\beta}$ aligned with $\vec{r}_{\beta\mu}$. Thus, $\mu_{\rm eff}$ is nonzero even in the zero-overlap limit, meaning that the smooth interactions are *not* completely smooth, but they give rise to much smaller maximum friction coefficient than for similar two-particle configurations with rough interactions.

We find that $\mu_{\text{eff}}^{\text{m}} = 0.190$ obtained in Section 9.3.3 is consistent with the maximum friction we measure by varying the *x*-component of $\vec{r}_{\beta r,\mu t}$ with the same \hat{y} component used in the starred configuration, $\mu_{\text{eff}}^{\text{max}} = 0.190$, marked with an "x" in Figure 9.19(e).

Acknowledgements

The authors acknowledge funding from NSF Grant Nos. BMMB-2029756 (C.O. and A.M.), BMMB-2414268 (C.O. and A.M.), CBET-2333222 (C.O.), CBET-2333223 (M.S.), and NIH Grant Nos. T32 GM 149438 (A.M.) and R01 CA276392 (C.O. and D.W.). This work was also supported by the High Performance Computing facilities operated by Yale's Center for Research Computing. The authors thank Luis Javier Perez-Lorenzo, Gregory Douglas Penn, and Sven Witthaus for their help in making the image in Figure 9.1(b).

References

- 1. M. L. Manning, Essay: Collections of deformable particles present exciting challenges for soft matter and biological physics, *Phys. Rev. Lett.*, 2023, **130**, 130002.
- 2. D. B. Khismatullin, The cytoskeleton and deformability of white blood cells, in *Current Topics in Membranes, Current Topics in Membranes*, Academic Press, 2009, vol. 64, ch. 3, pp. 47–111.
- 3. Y. Cheng, J. D. Treado, B. F. Lonial, P. Habdas, E. R. Weeks, M. D. Shattuck and C. S. O'Hern, Hopper flows of deformable particles, *Soft Matter*, 2022, **18**, 8071.
- 4. Y. Yuan, Z. Zeng, Y. Xing, H. Yuan, S. Zhang, W. Kob and Y. Wang, From creep to flow:Granular materials under cyclic shear, *Nat. Commun.*, 2024, **15.** 3866.
- 5. M. Merkel and M. L. Manning, A geometrically controlled rigidity transition in a model for confluent 3d tissues, *New J. Phys.*, 2018, **20**, 022002.
- 6. E. Dressaire and A. Sauret, Clogging of microfluidic systems, *Soft Matter*, 2016, **13**, 37.
- 7. T. E. Angelini, E. Hannezo, X. Trepat, M. Marquez, J. J. Fredberg and D. A. Weitz, Glass-like dynamics of collective cell migration, *Proc. Natl. Acad. Sci.*, 2011, **108**, 4714.
- 8. T. Lecuit and P.-F. Lenne, Cell surface mechanics and the control of cell shape, tissue patterns and morphogenesis, *Nat. Rev. Mol. Cell Biol.*, 2007, **8**, 633.
- 9. S. Stupkiewicz, M. J. Lewandowski and J. Lengiewicz, Micromechanical analysis of friction anisotropy in rough elastic contacts, *Int. J. Solids Struct.*, 2014, 51, 3931.
- 10. K. L. Johnson, Contact Mechanics, Cambridge University Press, 1987.
- 11. W. Liu, S. Li, A. Baule and H. A. Makse, Adhesive loose packings of small dry particles, *Soft Matter*, 2015, **11**, 6492.
- 12. M. Mailman, C. F. Schreck, C. S. O'Hern and B. Chakraborty, Jamming in systems composed of frictionless ellipse-shaped particles, *Phys. Rev. Lett.*, 2009, **102**, 255501.
- 13. R. Kawamoto, E. Andò, G. Viggiani and J. E. Andrade, Level set discrete element method for three-dimensional computations with triaxial case study, *J. Mech. Phys. Solids*, 2016, **91**, 1.
- 14. J. Duriez and C. Galusinski, A Level Set-Discrete Element Method in YADE for numerical, micro-scale, geomechanics with refined grain shapes, *Comput and Geosci*, 2021, 157, 104936.
- 15. J. T. Clemmer, J. M. Monti and J. B. Lechman, A soft departure from jamming: The compaction of deformable granular matter under high pressures, *Soft Matter*, 2024, **20**, 1702.
- 16. T.-L. Vu, J. Barés, S. Mora and S. Nezamabadi, Numerical simulations of the compaction of assemblies of rubberlike particles: A quantitative comparison with experiments, *Phys. Rev. E*, 2019, **99**, 062903.

17. S. Nezamabadi, T. H. Nguyen, J.-Y. Delenne and F. Radjai, Modeling soft granular materials, *Granul. Matter*, 2016, **19**, 8.

- 18. D. Cantor, M. Cárdenas-Barrantes, I. Preechawuttipong, M. Renouf and E. Azéma, Compaction model for highly deformable particle assemblies, *Phys. Rev. Lett.*, 2020, **124**, 208003.
- 19. D. J. Durian, Foam mechanics at the bubble scale, *Phys. Rev. Lett.*, 1995, 75, 4780.
- 20. P. V. Petkov and B. P. Radoev, Statics and dynamics of capillary bridges, *Colloids Surf.*, *A*, 2014, **460**, 18.
- 21. J. Bostwick and P. Steen, Stability of constrained capillary surfaces, *Annu. Rev. Fluid Mech.*, 2015, 47, 539.
- 22. R. Saye and J. Sethian, Multiscale modelling of evolving foams, *J. Comput. Phys.*, 2016, 315, 273.
- 23. K. A. Brakke, The surface evolver, Exp. Math., 1992, 1, 141.
- 24. A. Virozub, N. Haimovich and S. Brandon, Three-dimensional simulations of liquid bridges between two cylinders: Forces, energies, and torques, *Langmuir*, 2009, **25**, 12837.
- 25. F. Andrade, H. Al-Qureshi and D. Hotza, Measuring the plasticity of clays: A review, *Appl. Clay Sci.*, 2011, **51**, 1.
- 26. J. Richeton, S. Ahzi, K. Vecchio, F. Jiang and R. Adharapurapu, Influence of temperature and strain rate on the mechanical behavior of three amorphous polymers: Characterization and modeling of the compressive yield stress, *Int. J. Solids Struct.*, 2006, 43, 2318.
- 27. A. Boromand, A. Signoriello, F. Ye, C. S. O'Hern and M. D. Shattuck, Jamming of deformable polygons, *Phys. Rev. Lett.*, 2018, **121**, 248003.
- 28. D. Wang, J. D. Treado, A. Boromand, B. Norwick, M. P. Murrell, M. D. Shattuck and C. S. O'Hern, The structural, vibrational, and mechanical properties of jammed packings of deformable particles in three dimensions, *Soft Matter*, 2021, 17, 9901.
- 29. J. D. Treado, D. Wang, A. Boromand, M. P. Murrell, M. D. Shattuck and C. S. O'Hern, Bridging particle deformability and collective response in soft solids, *Phys. Rev. Mater.*, 2021, 5, 055605.
- 30. J. D. Treado, A. B. Roddy, G. Théroux-Rancourt, L. Zhang, C. Ambrose, C. R. Brodersen, M. D. Shattuck and C. S. O'Hern, Localized growth and remodelling drives spongy mesophyll morphogenesis, *J. R. Soc. Interface*, 2022, **19**, 20220602.
- 31. A. T. Ton, A. K. MacKeith, M. D. Shattuck and C. S. O'Hern, Mechanical plasticity of cell membranes enhances epithelial wound closure, *Phys. Rev. Res.*, 2024, **6**, L012036.
- 32. Cheng Y., Lonial B. F., Sista S., Meer D. J., Hofert A., Weeks E. R., Shattuck M. D., and O'Hern C. S., Flow and clogging of capillary droplets, *Soft Matter*, 2024, **20**, 8036.
- 33. Arfaee M., Kluin J. and Overvelde J. T., Modeling the behavior of elastic pouch motors, in *2023 IEEE International Conference on Soft Robotics* (*RoboSoft*), 2023, pp. 1–6.

- 34. K. Keren, Z. Pincus, G. M. Allen, E. L. Barnhart, G. Marriott, A. Mogilner and J. A. Theriot, Mechanism of shape determination in motile cells, *Nature*, 2008, **453**, 475.
- 35. A. Vaziri, Mechanics of highly deformed elastic shells, *Thin-Walled Struct.*, 2009, 47, 692.
- 36. J. N. Thon, H. Macleod, A. J. Begonja, J. Zhu, K.-C. Lee, A. Mogilner, J. H. Hartwig and J. E. Italiano, Microtubule and cortical forces determine platelet size during vascular platelet production, *Nat. Commun.*, 2012, 3, 852.
- 37. P. B. Umbanhowar, V. Prasad and D. A. Weitz, Monodisperse Emulsion Generation via Drop Break Off in a Coflowing Stream, *Langmuir*, 2000, **16**, 347.
- 38. M. A. C. Teixeira, S. Arscott, S. J. Cox and P. I. C. Teixeira, What is the shape of an air bubble on a liquid surface?, *Langmuir*, 2015, **31**, 13708.
- 39. Y. Zheng, D. Wang, G. Beeghly, C. Fischbach, M. D. Shattuck and C. S. O'Hern, Computational modeling of the physical features that influence breast cancer invasion into adipose tissue, *APL Bioeng.*, 2024, **8**, 036104.
- 40. A. D. Berman, W. A. Ducker and J. N. Israelachvili, Origin and characterization of different stickslip friction mechanisms, *Langmuir*, 1996, **12**, 4559.
- 41. S. Papanikolaou, C. S. O'Hern and M. D. Shattuck, Isostaticity at frictional jamming, *Phys. Rev. Lett.*, 2013, **110**, 198002.
- 42. Puttock M. and Thwaite E., Elastic compression of spheres and cylinders at point and line contact (Commonwealth Scientific and Industrial Research Organization Melbourne, 1969).
- 43. Y. Li, X.-L. Gao, S. Horner and J. Zheng, Analytical models for the impact of a solid sphere on a fluid-filled spherical shell incorporating the stress wave propagation effect and their applications to blunt head impacts, *Int. J. Mech. Sci.*, 2017, **130**, 586.
- 44. E. Bitzek, P. Koskinen, F. Gähler, M. Moseler and P. Gumbsch, Structural relaxation made simple, *Phys. Rev. Lett.*, 2006, **97**, 170201.
- 45. Fang M. C., Closed form for half-area overlap offset of 2 unit disks, *arXiv*, 2024, arXiv:2403.10529.
- 46. A. P. Thompson, S. J. Plimpton and W. Mattson, General formulation of pressure and stress tensor for arbitrary many-body interaction potentials under periodic boundary conditions, *J. Chem. Phys*, 2009, **131**, 154107.
- 47. M. J. Louwerse and E. J. Baerends, Calculation of pressure in case of periodic boundary conditions, *Chem. Phys. Lett.*, 2006, **421**, 138.
- 48. S. Zhang, W. Jin, D. Wang, D. Xu, J. Zhang, M. D. Shattuck and C. S. O'Hern, Local and global measures of the shear moduli of jammed disk packings, *Phys. Rev. E*, 2023, **107**, 054903.
- 49. A. I. Murdoch, A Critique of Atomistic Definitions of the Stress Tensor, *J. Elast.*, 2007, **88**, 113.
- 50. J. H. Irving and J. G. Kirkwood, The statistical mechanical theory of transport processes. IV. The equations of hydrodynamics, *J. Chem. Phys.*, 1950, **18**, 817.

51. K. Shi, E. R. Smith, E. E. Santiso and K. E. Gubbins, A perspective on the microscopic pressure (stress) tensor: History, current understanding, and future challenges, *J. Chem. Phys.*, 2023, **158**, 040901.

- 52. C. S. O'Hern, L. E. Silbert, A. J. Liu and S. R. Nagel, Jamming at zero temperature and zero applied stress: The epitome of disorder, *Phys. Rev. E*, 2003, **68**, 011306.
- 53. A. V. Tkachenko and T. A. Witten, Stress propagation through frictionless granular material, *Phys. Rev. E*, 1999, **60**, 687.
- 54. T. C. Lubensky, C. L. Kane, X. Mao, A. Souslov and K. Sun, Corrigendum: Phonons and elasticity in critically coordinated lattices, *Rep. Prog. Phys.*, 2015, **78**, 109501.
- 55. K. VanderWerf, W. Jin, M. D. Shattuck and C. S. O'Hern, Hypostatic jammed packings of frictionless nonspherical particles, *Phys. Rev. E*, 2018, **97**, 012909.
- 56. Y. Yuan, K. VanderWerf, M. D. Shattuck and C. S. O'Hern, Jammed packings of 3d superellipsoids with tunable packing fraction, coordination number, and ordering, *Soft Matter*, 2019, **15**, 9751.
- 57. C. Brito, H. Ikeda, P. Urbani, M. Wyart and F. Zamponi, Universality of jamming of nonspherical particles, *Proc. Natl. Acad. Sci.*, 2018, **115**, 11736.
- 58. M. P. Allen and D. J. Tildesley, *Computer Simulation of Liquids*, Oxford University Press, 2017.
- 59. K. VanderWerf, A. Boromand, M. D. Shattuck and C. S. O'Hern, Pressure dependent shear response of jammed packings of frictionless spherical particles, *Phys. Rev. Lett.*, 2020, **124**, 038004.
- 60. J. Zhang, D. Wang, W. Jin, A. Xia, N. Pashine, R. Kramer-Bottiglio, M. D. Shattuck and C. S. O'Hern, Designing the pressure-dependent shear modulus using tessellated granular metamaterials, *Phys. Rev. E*, 2023, **108**, 034901.
- 61. S. Dagois-Bohy, B. P. Tighe, J. Simon, S. Henkes and M. van Hecke, Soft-sphere packings at finite pressure but unstable to shear, *Phys. Rev. Lett.*, 2012, **109**, 095703.